The Astrophysical Journal, 993:56 (14pp), 2025 November 1 https://doi.org/10.3847/1538-4357/ae0463


# The Epoch of Reionization 21 cm Bispectrum at $z = 8.2$ from MWA Data. I. Foregrounds and Preliminary Upper Limits

Sukhdeep Singh Gill[1], Somnath Bharadwaj[1], Khandakar Md Asif Elahi[2], Shiv K. Sethi[3], and Akash Kumar Patwa[3]
[1] Department of Physics, Indian Institute of Technology Kharagpur, Kharagpur 721 302, India; sukhdeepsingh5ab@gmail.com
[2] Centre for Strings, Gravitation and Cosmology, Department of Physics, Indian Institute of Technology Madras, Chennai 600036, India
[3] Raman Research Institute, C. V. Raman Avenue, Sadashivanagar, Bengaluru 560080, India
*Received 2025 July 7; revised 2025 August 16; accepted 2025 September 3; published 2025 October 24*

## Abstract

We attempt to measure the $z = 8.2$ Epoch of Reionization (EoR) 21 cm bispectrum (BS) using Murchison Widefield Array 154.2 MHz data. We find that $B(k_{1\perp}, k_{2\perp}, k_{3\perp}, k_{1\parallel}, k_{2\parallel})$, the 3D cylindrical BS, exhibits a foreground wedge, similar to $P(k_{1\perp}, k_{1\parallel})$, the 21 cm cylindrical power spectrum. However, the BS foreground wedge, which depends on $(k_{1\perp}, k_{1\parallel})$, $(k_{2\perp}, k_{2\parallel})$, and $(k_{3\perp}, k_{3\parallel})$, the three sides of a triangle, is more complicated. Considering various foreground avoidance scenarios, we identify the region where all three sides are outside the foreground wedge as the EoR window for the 21 cm BS. However, the EoR window is contaminated by a periodic pattern of spikes that arises from the periodic pattern of missing frequency channels in the data. We evaluate the binned 3D spherical BS for triangles of all possible sizes and shapes, and present results for $\Delta^3$, the mean-cube brightness temperature fluctuations. The best $2\sigma$ upper limits we obtain for the EoR 21 cm signal are $\Delta^3_{\rm UL} = (1.81 \times 10^3)^3\,{\rm mK}^3$ at $k_1 = 0.008\,{\rm Mpc}^{-1}$ and $\Delta^3_{\rm UL} = (2.04 \times 10^3)^3\,{\rm mK}^3$ at $k_1 = 0.012\,{\rm Mpc}^{-1}$ for equilateral and squeezed triangles, respectively. These are foreground dominated and are many orders of magnitude larger than the predicted EoR 21 cm signal ($\sim 10^3\,{\rm mK}^3$).

*Unified Astronomy Thesaurus concepts:* Reionization (1383); Astronomy data analysis (1858); Radio interferometry (1346); H I line emission (690); Interferometric correlation (807); Diffuse radiation (383); Observational cosmology (1146); Non-Gaussianity (1116)

## 1. Introduction

The Epoch of Reionization (EoR) marks the phase transition of the Universe when the first luminous sources reionized the diffuse neutral hydrogen (H I) in the intergalactic medium (IGM). There are numerous indirect observations, such as the cosmic microwave background (E. Komatsu et al. 2011; D. Larson et al. 2011; Planck Collaboration et al. 2016), the absorption spectra of quasars (R. H. Becker et al. 2001; X. Fan et al. 2003; R. L. White et al. 2003; R. Barnett et al. 2017), and the luminosity function of Ly$\alpha$ emitters (M. Ouchi et al. 2010; M. Trenti et al. 2010; H. Jensen et al. 2013; T. R. Choudhury et al. 2015; R. Bouwens 2016; K. Ota et al. 2017), that constrain the EoR. Nonetheless, our understanding of the physical processes occurring during the EoR remains quite limited, and precisely constraining its duration and underlying mechanisms continues to be an ongoing research endeavor (S. Mitra et al. 2015; G. Kulkarni et al. 2019; L. C. Keating et al. 2020; S. E. I. Bosman et al. 2022; F. Melia 2024; J. B. Muñoz et al. 2024; H. Umeda et al. 2024; C. Cain et al. 2025a, 2025b; C. Papovich et al. 2025; Y. Qin et al. 2025; A. Runnholm et al. 2025; J. Witstok et al. 2025). Observation of the redshifted H I 21 cm radiation is a very promising probe of the EoR (S. Bharadwaj & S. S. Ali 2004; A. Loeb & M. Zaldarriaga 2004; S. R. Furlanetto 2006; J. R. Pritchard & A. Loeb 2012; S. Zaroubi 2013), and considerable efforts are underway to carry out such observations using radio telescopes such as the upgraded Giant Metrewave Radio Telescope[4] (G. Swarup et al. 1991; Y. Gupta et al. 2017), the Murchison Widefield Array (MWA;[5] S. J. Tingay et al. 2013), the Low Frequency Array[6] (M. P. van Haarlem et al. 2013), the Hydrogen Epoch of Reionization Array (HERA;[7] D. R. DeBoer et al. 2017), and the upcoming Square Kilometre Array–Low[8] (L. Koopmans et al. 2015). The major obstacle for these observations lies in foregrounds that are 4–5 orders of magnitude larger than the expected 21 cm signal (S. S. Ali et al. 2008). Currently, the best upper limits on the EoR 21 cm mean-squared brightness temperature fluctuations come from the HERA experiment, which are $[\Delta^2] \leqslant (30.76)^2\,{\rm mK}^2$ at $k = 0.192\,h\,{\rm Mpc}^{-1}$ at $z = 7.9$, and $[\Delta^2] \leqslant (95.74)^2\,{\rm mK}^2$ at $k = 0.256\,h\,{\rm Mpc}^{-1}$ at $z = 10.4$ (Z. Abdurashidova et al. 2022).

Much attention has been focused on the 21 cm power spectrum (PS), or equivalently, on $[\Delta^2]$ the mean-squared brightness temperature fluctuations mentioned earlier. Although these are adequate to completely quantify the statistics of a Gaussian random field, the 21 cm EoR signal is predicted to be highly non-Gaussian (S. Bharadwaj & S. K. Pandey 2005; R. Mondal et al. 2015), and it is necessary to consider higher-order statistics such as the bispectrum (BS). In an early work, S. Bharadwaj & S. K. Pandey (2005) used a simple analytical model for the ionized bubble distribution to calculate the EoR 21 cm BS, which was predicted to be negative. Since then, the EoR 21 cm BS has been extensively

[4] http://www.gmrt.ncra.tifr.res.in
[5] https://www.mwatelescope.org/
[6] https://www.astron.nl/telescopes/lofar/
[7] https://reionization.org/
[8] www.skao.int/en

studied using simulated H I 21 cm maps (S. Yoshiura et al. 2015; H. Shimabukuro et al. 2016; S. Majumdar et al. 2018, 2020; C. M. Trott et al. 2019; A. Hutter et al. 2020; A. Saxena et al. 2020; C. A. Watkinson et al. 2021; S. S. Gill et al. 2024; C. S. Murmu et al. 2024; J. Raste et al. 2024). The measurements of the EoR 21 cm BS can be used to tighten the constraints on the EoR models (H. Tiwari et al. 2022; C. A. Watkinson et al. 2022), and probe the IGM physics (M. Kamran et al. 2021a, 2021b, 2022; C. A. Watkinson et al. 2021). Moreover, the BS will be crucial in validating any detection of the EoR 21 cm PS. In addition to the BS, the skewness and kurtosis have also been proposed to quantify the level of non-Gaussianity (G. J. A. Harker et al. 2009; H. Shimabukuro et al. 2015; C. A. Watkinson & J. R. Pritchard 2015), but being one-point statistics, they only capture limited information. The skew spectrum has been proposed as an alternative to the BS to study the non-Gaussianity in the EoR 21 cm signal (Q.-B. Ma & L. Peng 2023). It is also possible to quantify non-Gaussianity by studying the geometry and topology of the EoR H I distribution (S. Bag et al. 2018, 2019).

To the best of our knowledge, there has been only one previous work that aims to measure the EoR 21 cm BS. C. M. Trott et al. (2019) analyzed 21 hr of 167–197 MHz ($z = 6.2$–$7.5$) MWA Phase II EoR project data to estimate the 21 cm BS for a few triangle configurations. They found that for large-scale isosceles triangles, the thermal noise limit is achieved in 10 hr of observation, whereas the equilateral configurations are strongly foreground dominated, with measured values several orders of magnitude above the noise predictions. The upper limit on the BS is measured to be $\sim 10^{12}$ mK$^3$ Mpc$^6$ on large scales. The authors argued that by choosing triangle configurations that minimize the foreground bias, BS detections could be achieved with only a few hundred hours of MWA observations, potentially requiring less time than the equivalent PS detection.

S. Bharadwaj & S. K. Pandey (2005) proposed three visibility correlations to measure the EoR 21 cm BS from radio-interferometric data. In the present paper, we implement this to measure the BS using ≈17 minutes of 154.2 MHz MWA data with (R.A., decl.) = (6.°1, −26.°7). The implementation is carried out in stages, which we briefly outline below. S. S. Gill et al. (2025, hereafter Paper I) proposed and validated an efficient technique to compute the three visibility correlations and estimate the angular BS $B_A(\ell_1, \ell_2, \ell_3)$ of the sky signal from radio-interferometric data at a single frequency $\nu$. S. S. Gill & S. Bharadwaj (2025b, hereafter Paper II) generalized this for multifrequency data to estimate the multifrequency angular BS (MABS) $B_A(\ell_1, \ell_2, \ell_3, \nu_1, \nu_2, \nu_3)$. This, in turn, was used to estimate the cylindrical BS $B(k_{1\perp}, k_{2\perp}, k_{3\perp}, k_{1\parallel}, k_{2\parallel})$ and then the spherical BS $B(k_1, k_2, k_3)$ (S. S. Gill & S. Bharadwaj 2025a) of the three-dimensional (3D) 21 cm signal.

It is now well accepted that foreground contamination in the estimated EoR 21 cm cylindrical PS $P(k_{1\perp}, k_{1\parallel})$ is largely confined within the "foreground wedge" (A. Datta et al. 2010; M. F. Morales et al. 2012; A. R. Parsons et al. 2012; C. M. Trott et al. 2012; H. Vedantham et al. 2012; S. G. Murray & C. M. Trott 2018). The region of the $(k_{1\perp}, k_{1\parallel})$ plane outside the foreground wedge, the "EoR window," is relatively free of foreground contamination and can be used to measure the EoR 21 cm PS. In this work, we provide a detailed analysis of the cylindrical BS to elucidate the impact of foreground contamination. In particular, we investigate whether it is possible to identify a foreground wedge and an EoR window for the 21 cm cylindrical BS.

In this paper, we present a comprehensive analysis of the spherical BS considering all possible triangle configurations that arise from the present observational data. We use this to place upper limits on the mean-cubed 21 cm brightness temperature fluctuations, and compare these with the corresponding upper limits on the mean-squared brightness temperature fluctuations obtained from the same data.

The structure of the paper is as follows. In Section 2, we describe the observational data and the simulation of system noise. Section 3 provides a brief overview of the BS statistic, including its estimation and parameterization. The main results are presented in Section 4. Finally, Section 5 summarizes the findings and concludes the paper.

The cosmological parameters used in this work are taken from Planck Collaboration et al. (2020).

## 2. Data

We used data from the Phase II MWA drift-scan observations (project ID: G0031) described in A. K. Patwa et al. (2021). These observations were made at a fixed decl. of −26.°7, corresponding to the zenith, and span the range of R.A. = [349°,70.°3], covering a total of 81.°3. Each pointing center (PC) was observed for approximately 2 minutes, with 162 discrete PCs spaced at an interval of 0.°5 along the R.A. In this work, we restrict our analysis to a single PC corresponding to (R.A., decl.) = (6.°1, −26.°7). The visibility data was initially recorded at a time resolution of 0.5 s, and subsequently averaged to 10 s resolution, which gives 11 distinct time stamps for each PC. For this PC, the data was further averaged over $N_{\rm nights} = 9$ nights of observations, which gives an effective integration time of $t_{\rm int} = N_{\rm nights} \times 10\,{\rm s} = 90\,{\rm s}$ for each time stamp. We have a total observation time of ≈17 minutes for this PC.

The observation comprises $N_c = 768$ frequency channels, with frequency resolution of $\Delta\nu_c = 40$ kHz, yielding a total bandwidth of $B_{\rm bw} = 30.72$ MHz centered at frequency $\nu_c = 154.2$ MHz. This data set probes the H I 21 cm line over the redshift range of [7.4, 9.2], with a central redshift of $z = 8.2$. The full bandwidth is divided into 24 coarse bands, each containing 32 fine channels. For each coarse band, four edge channels at both ends and one central channel are flagged. The resulting flagging pattern is periodic with a frequency spacing of 1.28 MHz. Additionally, at each baseline, different channels may be flagged to avoid radio frequency interference. The baselines in the data are mostly (∼99%) within $U = 250$ (S. Chatterjee et al. 2024). Here, we restrict our analysis to baselines in the range of $5 \leqslant U \leqslant 277$. We have validated our 3D BS estimator on this data in Paper II, using the same baseline distribution, frequency bandwidth, and flagging scheme. For each baseline $\boldsymbol{U}$ and frequency $\nu$, we have separate measurements for two orthogonal polarizations, namely LL and RR, denoted as $\mathcal{V}_{\rm LL}(\boldsymbol{U}, \nu)$ and $\mathcal{V}_{\rm RR}(\boldsymbol{U}, \nu)$, respectively. We treat these as independent measurements and combine them when gridding the visibility data.

We note that the same data were used in S. Chatterjee et al. (2024) and K. M. A. Elahi et al. (2025) to estimate the multifrequency angular PS (MAPS) $C_\ell(\Delta\nu)$ and the cylindrical PS $P(k_{1\perp}, k_{1\parallel})$, considering an approach that is very

similar to the one adopted here to estimate the MABS and the cylindrical BS. Furthermore, the baseline distribution, frequency coverage, and flagging pattern of the simulated data used to validate our BS estimators in Paper I and Paper II exactly match those of the data that has been analyzed here.

Each visibility measurement also includes a system noise contribution. To quantify the system noise contribution to the BS, we perform dedicated "noise-only" simulations. Following S. Chatterjee et al. (2024), we have modeled the noise in the real and imaginary parts of the visibilities as Gaussian random variables (A. R. Thompson et al. 2017) with zero mean and standard deviation:

$$\sigma_N = \frac{1}{\eta_Q} \frac{\sqrt{2}\, k_B T_{\rm sys}}{A_{\rm eff} \sqrt{\Delta\nu_c t_{\rm int}}}\,, \tag{1}$$

where the effective area $A_{\rm eff} = 21.4\,{\rm m}^2$, system temperature $T_{\rm sys} = 400$ K, quantization efficiency $\eta_Q = 1$, and integration time $t_{\rm int} = 90$ s yield $\sigma_N \approx 20$ Jy (A. K. Patwa et al. 2021). Our simulations assume the noise to be uncorrelated across the visibility data in different baselines, frequency channels, time stamps, and polarizations. Simulated visibilities are generated using the same baseline and frequency configurations of the actual data and incorporating identical flagging information. To ensure statistical robustness, we produce 50 independent noise realizations. These simulations are used to quantify the uncertainty in the measured BS due to system noise.

## 3. Methodology

We employ our recently developed estimator (Paper II) to compute the BS from $\mathcal{V}(\boldsymbol{U}, \nu)$, the radio-interferometric visibility data. While the detailed formulation and validation of the estimator can be found in Paper II, a concise overview of the procedure is presented here. The estimation proceeds in three main steps. In the first step, we evaluate the MABS, $B_A(\ell_1, \ell_2, \ell_3, \nu_1, \nu_2, \nu_3)$, by correlating three gridded visibilities across different baselines ($\boldsymbol{U}_1$, $\boldsymbol{U}_2$, $\boldsymbol{U}_3$) and frequencies ($\nu_1$, $\nu_2$, $\nu_3$). In the second step, we perform a 2D Fourier transform of the MABS to compute the 3D cylindrical BS. In the third step, we average triangles of different orientations to calculate the spherical BS. The following subsections detail the procedures and results for the first two steps. The results for the spherical BS are presented in the next section.

### 3.1. The MABS

The relation between the three visibility correlations and MABS is given by

$$\begin{aligned}&\langle \mathcal{V}(\boldsymbol{U}_1, \nu_1)\mathcal{V}(\boldsymbol{U}_2, \nu_2)\mathcal{V}(\boldsymbol{U}_3 + \Delta\boldsymbol{U}, \nu_3)\rangle \\ &= \left[\frac{\pi\theta_0^2 Q^3}{3} \exp(-\pi^2\theta_0^2 \Delta U^2/3)\right] \times B_A(\ell_1, \ell_2, \ell_3, \nu_1, \nu_2, \nu_3),\end{aligned} \tag{2}$$

where $\boldsymbol{U}_1 + \boldsymbol{U}_2 + \boldsymbol{U}_3 = 0$ forms a closed triangle, $\boldsymbol{\ell} = 2\pi\boldsymbol{U}$, and $\Delta\boldsymbol{U}$ is the deviation from a closed triangle configuration. Here, $Q = 2k_B/\lambda^2$ is the Rayleigh–Jeans factor, which converts brightness temperature to specific intensity, and $\theta_0 = 0.6\theta_{\rm FWHM}$, where $\theta_{\rm FWHM} \approx 24.^\circ68$ for the MWA primary beam. We use the values of $Q$ and $\theta_0$ at the central frequency $\nu_c$, assuming the bandwidth is sufficiently small. The normalization factor within the square brackets [...] in Equation (2) has been calculated analytically (Paper I) by approximating the MWA primary beam pattern as a Gaussian. The Gaussian approximation ignores the side lobes of the actual MWA primary beam pattern. To estimate the impact of this assumption, we have considered a situation where we approximate the MWA primary beam pattern using a product of sinc$^2$ functions, which exhibits side lobes. The results for this are presented in the Appendix. We find that the difference is less than 3% for small $\Delta U$, which is the range that is relevant for our analysis.

Paper II presents the binned MABS estimator, and validates it using simulated visibility data that exactly match the observation for which we now analyze the actual data. The procedure here is identical to that used in Paper II, so we do not present it here again. Briefly, we grid the visibilities on a square grid of spacing $\Delta U_g = \sqrt{\ln 2}/(\pi\theta_0) \approx 1$ in the $\boldsymbol{U}$-plane. We then divide the $\boldsymbol{U}$-plane into several concentric annular rings. Each combination of three annular rings provides an estimate of the binned MABS. We have evaluated the binned MABS estimator for all possible combinations of three rings. Note that some combinations of three rings do not contain any closed triangle $\boldsymbol{U}_1 + \boldsymbol{U}_2 + \boldsymbol{U}_3 = 0$ and are discarded.

The sky signal is assumed to be isotropic in the plane of the sky, which allows us to bin together triangles ($\boldsymbol{U}_1$, $\boldsymbol{U}_2$, $\boldsymbol{U}_3$), or equivalently ($\ell_1$, $\ell_2$, $\ell_3$), of the same shape and size but with different orientations. Here we obtain estimates of the MABS, $B_A(\ell_1, \ell_2, \ell_3, \nu_1, \nu_2, \nu_3)$, for 647 distinct ($\ell_1$, $\ell_2$, $\ell_3$) bins that together cover all possible triangle configurations for the present data. In addition to triangles of different orientations, each bin also includes triangles within a finite range of shapes and sizes, as determined by the widths of the annular rings. In the subsequent discussion, we refer to each bin, labeled ($\ell_1$, $\ell_2$, $\ell_3$) with $\ell_1 \geqslant \ell_2 \geqslant \ell_3$, as a "triangle configuration." We use $\ell_1$, the largest side, to quantify the size of the triangle configuration, and the sides span the range of $50 \leqslant \ell_1,\ \ell_2,\ \ell_3 \leqslant 1629$. Here we explicitly show the MABS for four representative triangle configurations, all of the same size ($\ell_1 = 711$) but of different shapes, namely equilateral, squeezed, stretched, and right-angle, shown from left to right in the top row of Figure 1. The corresponding ($\ell_1$, $\ell_2$, $\ell_3$) values are shown in the bottom row of the figure.

Considering the MABS $B_A(\ell_1, \ell_2, \ell_3, \nu_1, \nu_2, \nu_3)$, we assume that the 21 cm signal is ergodic along frequency, or equivalently, the line-of-sight (LoS) direction. As a result, the MABS depends only on the frequency separations, i.e., we can then express the MABS as $B_A(\ell_1, \ell_2, \ell_3, \Delta\nu_1, \Delta\nu_2)$, where $\Delta\nu_1 = \nu_1 - \nu_3$ and $\Delta\nu_2 = \nu_2 - \nu_3$. For any triangle configuration ($\ell_1$, $\ell_2$, $\ell_3$), we have discrete estimates of the MABS at a regular interval of $\Delta\nu_c = 40$ kHz over the range of $-B_{\rm bw}$ to $B_{\rm bw}$ in the ($\Delta\nu_1$, $\Delta\nu_2$) plane. However, the region $|\Delta\nu_2 - \Delta\nu_1| > B_{\rm bw}$ remains unsampled (Figure 2 of Paper II), and we restrict the analysis to the range of $-B_{\rm bw}/2$ to $B_{\rm bw}/2$ for ease of computation. Furthermore, the MABS exhibits the symmetry $B_A(\ell_1, \ell_2, \ell_3, -\Delta\nu_1, -\Delta\nu_2) = B_A(\ell_1, \ell_2, \ell_3, \Delta\nu_1, \Delta\nu_2)$, and it suffices to consider only the upper half-plane $-B_{\rm bw}/2 \leqslant \Delta\nu_1 \leqslant B_{\rm bw}/2$ and $0 \leqslant \Delta\nu_2 \leqslant B_{\rm bw}/2$, as in Figure 2.

Figure 2 presents the MABS, $B_A(\ell_1, \ell_2, \ell_3, \Delta\nu_1, \Delta\nu_2)$, as a function of ($\Delta\nu_1$, $\Delta\nu_2$). The four panels of this figure respectively correspond to the four ($\ell_1$, $\ell_2$, $\ell_3$) triangle configurations shown in Figure 1. We have estimates of the MABS across the entire ($\Delta\nu_1$, $\Delta\nu_2$) range shown here, and there are no missing frequency separations ($\Delta\nu_1$, $\Delta\nu_2$) due to

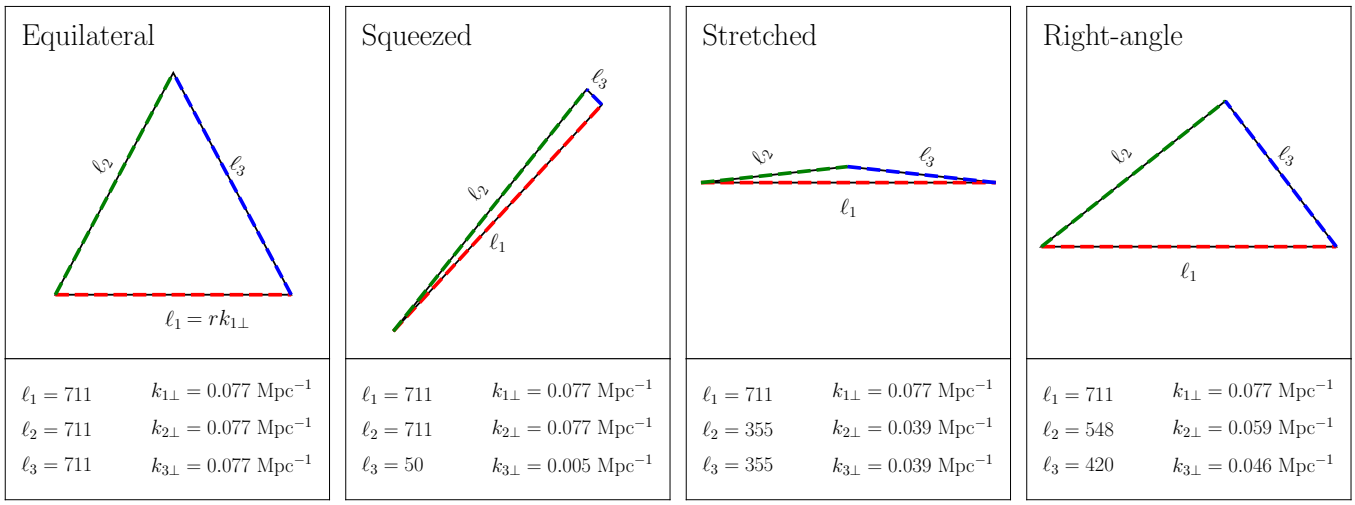


| | | | | | | | | |
|---|---|---|---|---|---|---|---|---|
| $\ell_1 = 711$ | $k_{1\perp} = 0.077$ Mpc$^{-1}$ | $\ell_1 = 711$ | $k_{1\perp} = 0.077$ Mpc$^{-1}$ | $\ell_1 = 711$ | $k_{1\perp} = 0.077$ Mpc$^{-1}$ | $\ell_1 = 711$ | $k_{1\perp} = 0.077$ Mpc$^{-1}$ |
| $\ell_2 = 711$ | $k_{2\perp} = 0.077$ Mpc$^{-1}$ | $\ell_2 = 711$ | $k_{2\perp} = 0.077$ Mpc$^{-1}$ | $\ell_2 = 355$ | $k_{2\perp} = 0.039$ Mpc$^{-1}$ | $\ell_2 = 548$ | $k_{2\perp} = 0.059$ Mpc$^{-1}$ |
| $\ell_3 = 711$ | $k_{3\perp} = 0.077$ Mpc$^{-1}$ | $\ell_3 = 50$ | $k_{3\perp} = 0.005$ Mpc$^{-1}$ | $\ell_3 = 355$ | $k_{3\perp} = 0.039$ Mpc$^{-1}$ | $\ell_3 = 420$ | $k_{3\perp} = 0.046$ Mpc$^{-1}$ |

**Figure 1.** Four triangle configurations—equilateral, squeezed, stretched, and right-angle—for which we explicitly present the MABS and the 3D cylindrical BS results. For each case, the numerical values of the triangle sides ($\ell_1$, $\ell_2$, $\ell_3$) together with the corresponding perpendicular wavenumbers $k_{1\perp} = \ell_1/r$, $k_{2\perp} = \ell_2/r$, and $k_{3\perp} = \ell_3/r$ are listed in the bottom row. These four cases are a small subset of the total of 669 distinct triangle configurations formed by all the ($\ell_1$, $\ell_2$, $\ell_3$) analyzed in this study.

the missing frequency channels $\nu$ of the MWA data. However, the number of triplets ($\nu_1$, $\nu_2$, $\nu_3$) corresponding to each combination of ($\Delta\nu_1$, $\Delta\nu_2$) exhibits a modulation due to the missing frequency channels, as shown in Figure 2 of Paper II. The sky signal here is foreground dominated, and we may interpret the estimated MABS as arising from the foregrounds. In all cases, we see that the MABS attains its maximum value ($\sim 10^6$ mK$^3$) at $\Delta\nu_1 = \Delta\nu_2 = 0$ and slowly declines with increasing frequency separations. The decline is not isotropic in ($\Delta\nu_1$, $\Delta\nu_2$), and is faster in the second quadrant compared to the first. The exact nature of the decline varies with the triangle shape, and we see that for the squeezed and stretched triangles, the red region (large value of the MABS) covers a wider range of ($\Delta\nu_1$, $\Delta\nu_2$) compared to the equilateral and right-angle triangles.

Figure 3 shows the MABS, $B_A(\ell_1, \ell_2, \ell_3, \Delta\nu_1, \Delta\nu_2)$, as a function of $\Delta\nu_1$ at fixed $\Delta\nu_2 = 0$. The different line styles correspond to different triangle configurations, as indicated in the figure legend. The maximum value of the MABS, at $\Delta\nu_1 = \Delta\nu_2 = 0$, varies in the range of $3.1 \times 10^6$–$2.4 \times 10^6$ mK$^3$, depending on the triangle configuration. In all cases, the MABS declines smoothly with increasing $|\Delta\nu_1|$ for $|\Delta\nu_1| \leqslant 5$ MHz, beyond which it continues to decline, but also exhibits some structures. This is particularly noticeable for the squeezed triangles, where the decline flattens out and shows small oscillations at $|\Delta\nu_1| \geqslant 5$ MHz. In no case does the MABS completely decorrelate (approach zero) within the $|\Delta\nu_1| \leqslant 15.36$ MHz range considered here. This behavior reflects the smooth spectral nature of the foregrounds, while the oscillations and other complex features that appear in the MABS are possibly due to additional chromaticity introduced by instrumental effects. Note the contrast with respect to the simulated 21 cm signal, where the MABS decorrelates to 95% of its peak value at $|\Delta\nu_1| = 2$ MHz, and is close to zero at $|\Delta\nu_1| \geqslant 2$ MHz (Figure 3 of Paper II).

### 3.2. The Cylindrical BS

The 3D cylindrical BS is obtained by performing a 2D Fourier transform of the MABS, as given by S. Bharadwaj & S. K. Pandey (2005):

$$B(k_{1\perp}, k_{2\perp}, k_{3\perp}, k_{1\parallel}, k_{2\parallel}) = r^4 r'^2 \int d(\Delta\nu_1) \int d(\Delta\nu_2) \times \exp[-ir'(k_{1\parallel}\Delta\nu_1 + k_{2\parallel}\Delta\nu_2)]\, B_A(\ell_1, \ell_2, \ell_3, \Delta\nu_1, \Delta\nu_2), \quad (3)$$

where $r$ is the comoving distance corresponding to the 21 cm signal received at $\nu_c$, which can be calculated from the redshift $z = \left(\frac{1420\ \text{MHz}}{\nu}\right) - 1$, and $r' = \frac{dr}{d\nu}$. Considering the wavenumber $\boldsymbol{k}$, here $\boldsymbol{k}_\perp = \boldsymbol{\ell}/r$ and $k_\parallel$ are respectively the components of $\boldsymbol{k}$ perpendicular and parallel to the LoS direction. The cylindrical BS $B(k_{1\perp}, k_{2\perp}, k_{3\perp}, k_{1\parallel}, k_{2\parallel})$ is a function of five independent variables, and $k_{3\parallel}$ is determined by the closed triangle condition $k_{3\parallel} = -k_{1\parallel} - k_{2\parallel}$. Here, the $\boldsymbol{k}_\perp$ value spans the range of $0.005\ \text{Mpc}^{-1} \leqslant k_{1\perp}, k_{2\perp}, k_{3\perp} \leqslant 0.177\ \text{Mpc}^{-1}$. The 2D Fourier transform of the MABS with respect to ($\Delta\nu_1$, $\Delta\nu_2$) (Equation (3)) introduces ripples along ($k_{1\parallel}$, $k_{2\parallel}$) in the 3D cylindrical BS due to the abrupt truncation at the boundaries $\pm 15.36$ MHz. We introduce a 2D Blackman–Nuttall window function (A. H. Nuttall 1981) that smoothly tapers the MABS at the boundaries, which suppresses the edge effects and mitigates the ripples along ($k_{1\parallel}$, $k_{2\parallel}$).

Figure 4 shows the 3D cylindrical BS $B(k_{1\perp}, k_{2\perp}, k_{3\perp}, k_{1\parallel}, k_{2\parallel})$ as a function of ($k_{1\parallel}$, $k_{2\parallel}$) with $(k_{1\perp}, k_{2\perp}, k_{3\perp}) = r^{-1}(\ell_1, \ell_2, \ell_3)$ fixed. Each column corresponds to a particular triangle configuration in the $\boldsymbol{k}_\perp$ plane, with the $(k_{1\perp}, k_{2\perp}, k_{3\perp})$ values shown in the bottom row of Figure 1. The available ($k_{1\parallel}$, $k_{2\parallel}$) values span the range of $[-4.61\ \text{Mpc}^{-1}, 4.61\ \text{Mpc}^{-1}]$ with a uniform spacing $\Delta k_\parallel = 0.012\ \text{Mpc}^{-1}$. The cylindrical BS has the symmetry $B(k_{1\perp}, k_{2\perp}, k_{3\perp}, k_{1\parallel}, k_{2\parallel}) = B(k_{1\perp}, k_{2\perp}, k_{3\perp}, -k_{1\parallel}, -k_{2\parallel})$ and it suffices to show the results for only the upper half-plane, as in Figure 4.

The top row of Figure 4 shows the cylindrical BS obtained from the MABS shown in Figure 2. The panels here consider the entire available ($k_{1\parallel}$, $k_{2\parallel}$) range. We see that the cylindrical BS peaks at $k_{1\parallel} = k_{2\parallel} = 0$ and falls rapidly at larger values of ($k_{1\parallel}$, $k_{2\parallel}$). In addition to the central peak, we also notice three dark bands that are respectively aligned with $k_{1\parallel} = 0$, $k_{2\parallel} = 0$,

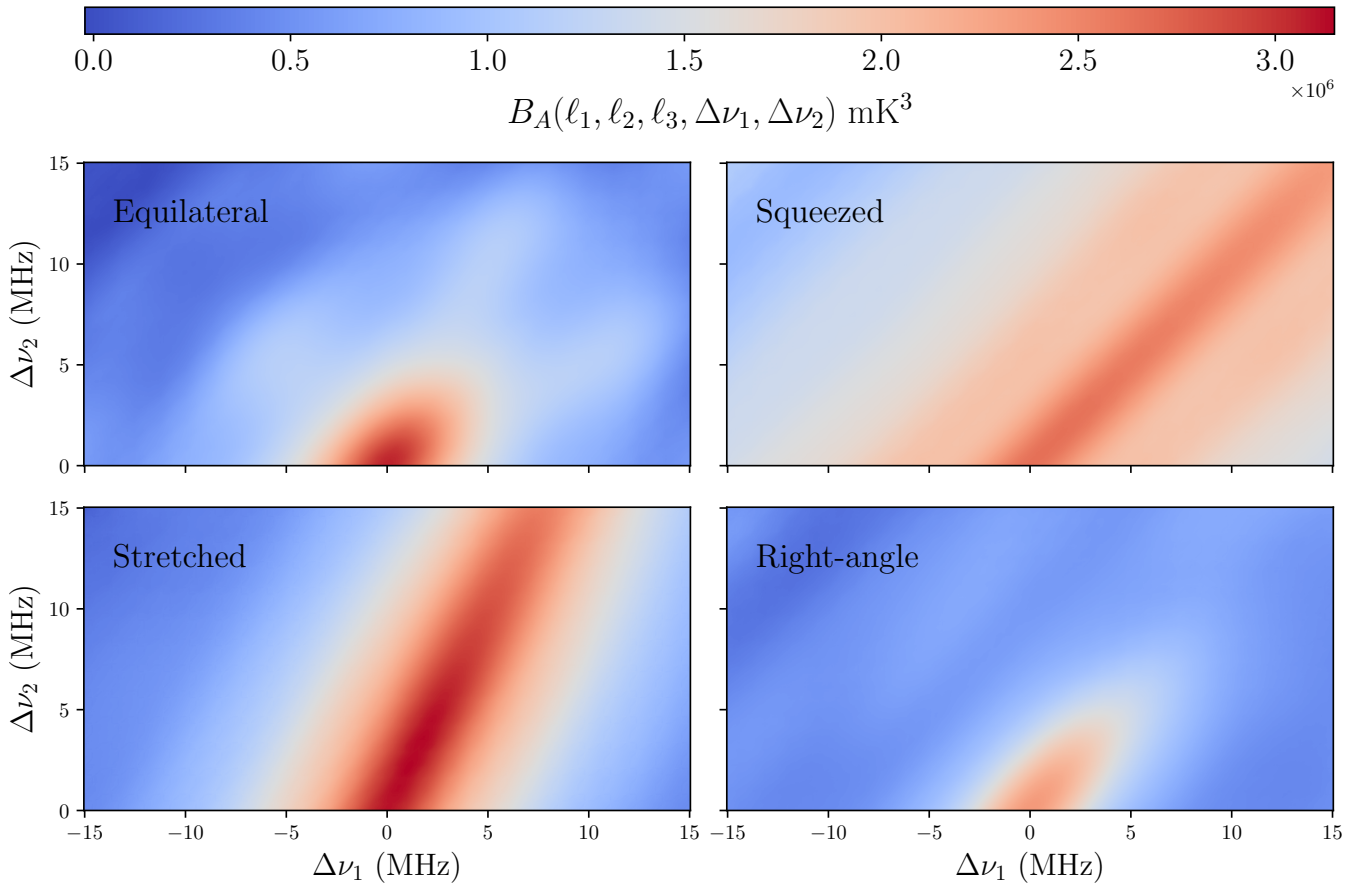


**Figure 2.** MABS $B_A(\ell_1, \ell_2, \ell_3, \Delta\nu_1, \Delta\nu_2)$ plotted as a function of $(\Delta\nu_1, \Delta\nu_2)$ for the four representative triangle configurations—equilateral (top left), squeezed (top right), stretched (bottom left), and right-angle (bottom right)—illustrated in Figure 1. The $\Delta\nu_1 - \Delta\nu_2$ plane is restricted to $|\nu_1|, |\nu_2| \leqslant B_{\rm bw}/2$, thereby excluding frequency separations that are not sampled. Only the upper half-plane, i.e., $-B_{\rm bw}/2 \leqslant \Delta\nu_1 \leqslant B_{\rm bw}/2$ and $0 \leqslant \Delta\nu_2 \leqslant B_{\rm bw}/2$, is displayed, owing to the symmetry $B_A(\ell_1, \ell_2, \ell_3, -\Delta\nu_1, -\Delta\nu_2) = B_A(\ell_1, \ell_2, \ell_3, \Delta\nu_1, \Delta\nu_2)$.

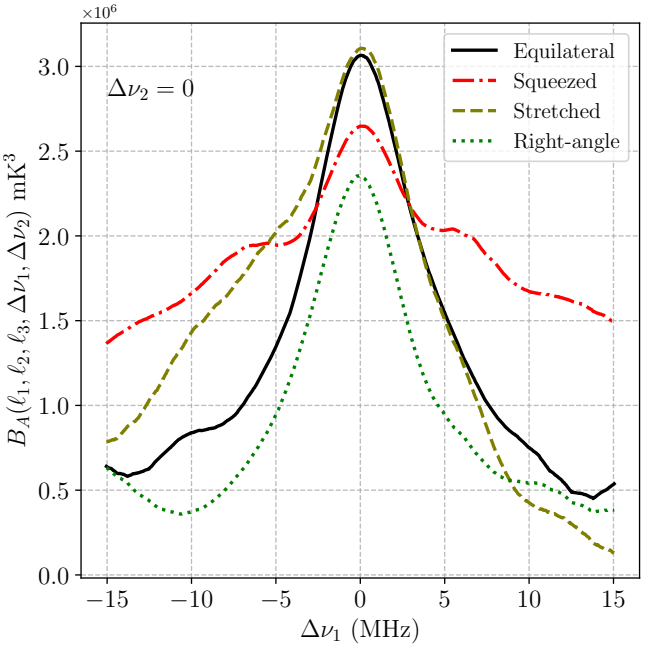


**Figure 3.** One-dimensional slices of the MABS plotted as a function of $\Delta\nu_1$ at fixed $\Delta\nu_2 = 0$, corresponding to each of the 2D MABS panels presented in Figure 2.

and $k_{1\parallel} = -k_{2\parallel}$ ($k_{3\parallel} = 0$). We identify these as the signature of spectrally smooth foreground contamination, which we will explore in greater detail in Section 3.3. In addition, we see a periodic square grid pattern that runs across the entire $(k_{1\parallel}, k_{2\parallel})$ plane. This has a spacing of $\delta k_\parallel = 0.29\,{\rm Mpc}^{-1}$, which arises from the periodic flagging present in the MWA data. A similar effect is also observed in the 3D cylindrical PS and has been studied in detail by K. M. A. Elahi et al. (2025).

The second row provides a zoomed-in view of the top row limited to the range of $-0.7\,{\rm Mpc}^{-1} \leqslant (k_{1\parallel}, k_{2\parallel}) \leqslant 0.7\,{\rm Mpc}^{-1}$, where the BS signal is concentrated. We see that overall, the BS has large values in this region compared to the large $(k_{1\parallel}, k_{2\parallel})$ that have been excluded from these panels. A prominent feature across all configurations is the bright central region, which is elongated, roughly along the antidiagonal direction. The direction of this elongation is orthogonal to that of the MABS shown in Figure 2. This is expected as the two are related through a Fourier transform (Equation (3)). The central bright region of the cylindrical BS is strongly foreground dominated, and the values of the cylindrical BS fall at larger $k_\parallel$. However, we find considerable foreground leakage outside the central bright region. The leakage shows a complex periodic pattern of positive and negative values, which is a combination of the spectral variation of the

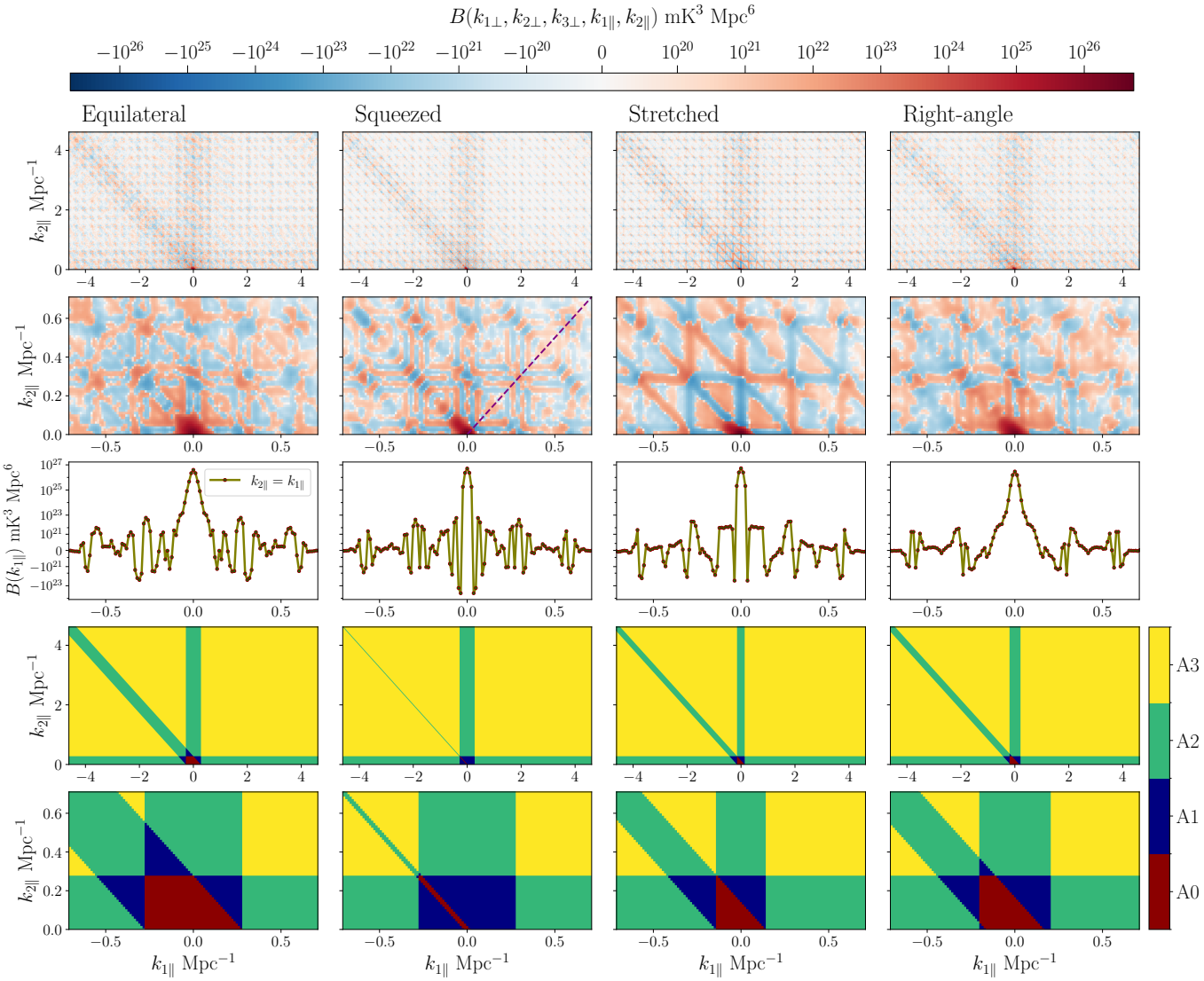


**Figure 4.** The 3D cylindrical BS $B(k_{1\perp}, k_{2\perp}, k_{3\perp}, k_{1\parallel}, k_{2\parallel})$ for the four triangle configurations $(k_{1\perp}, k_{2\perp}, k_{3\perp})$ shown in Figure 1. These results are obtained via a 2D Fourier transform (Equation (3)) of the MABS shown in Figure 2. The top row shows heat maps of the 3D BS over the entire $(k_{1\parallel}, k_{2\parallel})$ plane, while the second row zooms into the central region $-0.7\,\mathrm{Mpc}^{-1} \leqslant (k_{1\parallel}, k_{2\parallel}) \leqslant 0.7\,\mathrm{Mpc}^{-1}$. The third row shows 1D cuts along the diagonal $k_{1\parallel} = k_{2\parallel}$ (marked by a dashed brown line in the second row), plotted on a symmetric logarithmic scale with a linear range of $\pm 10^{21}$ mK$^3$ Mpc$^6$. The fourth row shows four distinct regions (A0, A1, A2, and A3) into which the $(k_{1\parallel}, k_{2\parallel})$ plane has been divided based on the number of triangle sides that are outside the foreground wedge, that is, $(k_{i\parallel} > [r/(r'\Delta\nu_c)]k_{i\perp})$. The bottom row provides a zoomed-in view of the fourth row.

foregrounds, the telescope's chromatic response, and the periodic pattern of missing frequency channels.

The third row shows the cylindrical BS $B(k_{1\perp}, k_{2\perp}, k_{3\perp}, k_{1\parallel}, k_{2\parallel})$ as a function of $k_{1\parallel}$ along the diagonal $k_{1\parallel} = k_{2\parallel}$, which is indicated by the dashed line in the panel for the squeezed triangle in the second row. In all cases, the peak value of the cylindrical BS is approximately $10^{27}$ mK$^3$ Mpc$^6$, and it decreases rapidly with increasing $k_{1\parallel}$, and subsequently exhibits an oscillatory behavior. The onset of these oscillations depends on the triangle configuration. For the equilateral triangle, the oscillations begin around $k_{1\parallel} \approx 0.1\,\mathrm{Mpc}^{-1}$, while they begin earlier ($\approx 0.03\,\mathrm{Mpc}^{-1}$) for the squeezed and stretched triangles, and later at $k_{1\parallel} \approx 0.2\,\mathrm{Mpc}^{-1}$ for the right-angle triangle. The amplitude of these oscillations is in the range of $10^{21}$–$10^{22}$ mK$^3$ Mpc$^6$, making them 5–6 orders of magnitude smaller than the maximum value of the BS. We find values in the range of $\pm(10^{19}$–$10^{20})$ mK$^3$ Mpc$^6$ in the region where the cylindrical BS appears to have values close to zero in the figure.

We have analyzed the noise-only simulations in exactly the same way as the actual data. First, we computed the MABS from each noise realization using Equation (2) and then evaluated the cylindrical BS via Equation (3). From 50 independent noise realizations, we calculated the rms of the resulting BS to obtain $\delta B_N$, which quantifies the expected statistical fluctuations due to system noise. We find that the estimated values of the cylindrical BS are considerably in excess of $\delta B_N$, indicating that all our results are foreground dominated.

### 3.3. The Foreground Wedge

The foreground contamination in the cylindrical PS $P(k_{1\perp}, k_{1\parallel})$ is largely confined within a wedge in the $(k_{1\perp}, k_{1\parallel})$ plane (A. Datta et al. 2010; M. F. Morales et al. 2012; A. R. Parsons et al. 2012; H. Vedantham et al. 2012;

S. G. Murray & C. M. Trott 2018). The wedge is defined by the condition $k_{1\parallel} \leqslant [k_{1\parallel}]_{\rm H}$, where the wedge boundary

$$[k_{1\parallel}]_{\rm H} = \left[\frac{r}{r'\Delta\nu_c}\right] k_{1\perp} = 3.51 k_{1\perp} \quad (4)$$

corresponds to a source at the horizon, and we have the value 3.51 for the data considered here. The region outside the wedge, the EoR window, is relatively free of foreground contamination. In principle, it is possible to overcome the problem of foreground contamination by adopting the technique of "foreground avoidance," which avoids the $(k_{1\perp}, k_{1\parallel})$ modes within the foreground wedge and only uses those in the EoR window to estimate the 21 cm PS.

The foreground wedge is a straightforward consequence of baseline migration, and we also expect this to manifest itself in the cylindrical BS $B(k_{1\perp}, k_{2\perp}, k_{3\perp}, k_{1\parallel}, k_{2\parallel})$ as well. However, the difficulty lies in visualizing this, the cylindrical BS being a function of five variables. Considering a fixed triangle configuration $(k_{1\perp}, k_{2\perp}, k_{3\perp})$, we have three distinct values for the wedge boundary,

$$([k_{1\parallel}]_{\rm H}, [k_{2\parallel}]_{\rm H}, [k_{3\parallel}]_{\rm H}) = \left[\frac{r}{r'\Delta\nu_c}\right] \times (k_{1\perp}, k_{2\perp}, k_{3\perp}), \quad (5)$$

and we have three conditions,

$$|k_{a\parallel}| \leqslant [k_{a\parallel}]_{\rm H}, \quad (6)$$

for $a = 1$, 2, and 3, respectively.

The fourth row of Figure 4 shows the region of $(k_{1\parallel}, k_{2\parallel})$ space that is denoted by Equation (6) for the four different triangle configurations considered here. In each panel, the vertical and horizontal green bands correspond to $-[k_{1\parallel}]_{\rm H} \leqslant k_{1\parallel} \leqslant [k_{1\parallel}]_{\rm H}$ and $0 \leqslant k_{2\parallel} \leqslant [k_{2\parallel}]_{\rm H}$, respectively. The antidiagonal green band is centered around $k_{3\parallel} = 0$, i.e., $k_{2\parallel} = -k_{1\parallel}$, and it has a width of $2 \times [k_{3\parallel}]_{\rm H}$. We expect the foreground contamination to be largely confined within the region covered by the green bands, and the yellow region is expected to be relatively free of foreground contamination. Here, we may interpret the yellow region as the EoR window. Considering the top row of Figure 4, we see the bands corresponding to $k_{1\parallel} = 0$, $k_{2\parallel} = 0$, and $k_{3\parallel} = 0$ are clearly visible for the actual data, and these regions show a high level of foreground contamination relative to the rest of the $(k_{1\parallel}, k_{2\parallel})$ plane. We notice that the EoR window is not as clean as expected, and we find considerable foreground leakage due to the periodic pattern of missing frequency channels.

The bottom row of Figure 4 provides a zoomed-in view of the central region, within the range of $-0.7\,{\rm Mpc}^{-1} \leqslant (k_{1\parallel}, k_{2\parallel}) \leqslant 0.7\,{\rm Mpc}^{-1}$ that matches the second row. Here we can clearly identify four distinct regions in the $(k_{1\parallel}, k_{2\parallel})$ plane, which we respectively label A0, A1, A2, and A3, as indicated in the figure. Here, A3 refers to the region where all three modes $(k_{1\perp}, k_{1\parallel})$, $(k_{2\perp}, k_{2\parallel})$, and $(k_{3\perp}, k_{3\parallel})$ avoid the foreground wedge. Similarly, A2, A1, and A0 refer to the regions where, respectively, only two, one, and zero modes avoid the foreground wedge. We expect foreground contamination to be the most severe in region A0, which corresponds to the bright central region in the panels of the second row. We expect the foreground contamination to diminish as we go from A0 to A3. As mentioned earlier, we refer to A3 as the EoR window for the cylindrical BS. Considering the fourth row, we see that the EoR window (A3) covers the largest fraction of the $(k_{1\parallel}, k_{2\parallel})$ plane, and the fraction shrinks successively as we move from A3 to A0. Table 1 shows the number of triangles corresponding to each of the four regions considered here. We see that 83.6% of the triangles are in the EoR window (A3), which is very promising for detecting the EoR 21 cm BS. Considering foreground avoidance, we need to discard only a small fraction of the triangles to avoid foreground contamination. Note that the values quoted in Table 1 refer to the total number of triangles used in our analysis, which is also the total number of triangles $(\boldsymbol{k}_1, \boldsymbol{k}_2, \boldsymbol{k}_3)$ available from the MWA data, and not just those shown in Figure 4.

Figure 5 shows a comparison of $B(k_{1\perp}, k_{1\parallel})$ the cylindrical BS with $P(k_{1\perp}, k_{1\parallel})$ the cylindrical PS estimates from K. M. A. Elahi et al. (2025), who have analyzed the same MWA data. The first two columns show $B(k_{1\perp}, k_{2\perp}, k_{3\perp}, k_{1\parallel}, k_{2\parallel})$ as a function of $(k_{1\perp}, k_{1\parallel})$ considering squeezed triangles for which $k_{2\perp} \approx k_{1\perp}$ and $k_{3\perp} \to 0$ (actually the minimum value $k_{3\perp} = 0.005\,{\rm Mpc}^{-1}$). The left and middle columns, respectively, consider $(k_{2\parallel} = k_{1\parallel}, k_{3\parallel} = -2k_{1\parallel})$ and $(k_{2\parallel} = -k_{1\parallel}, k_{3\parallel} = 0)$. The right column shows $P(k_{1\perp}, k_{1\parallel})$.

We first consider the upper row of Figure 5, which shows heat maps of $B(k_{1\perp}, k_{1\parallel})$ and $P(k_{1\perp}, k_{1\parallel})$. The foreground wedge is clearly visible in the right panel that shows $P(k_{1\perp}, k_{1\parallel})$. We also notice leakage beyond the wedge boundary $(k_{1\parallel} \geqslant [k_{1\parallel}]_{\rm H})$, particularly horizontal streaks along $k_{1\parallel}$ due to the periodic pattern of missing frequency channels. The panels showing $B(k_{1\perp}, k_{1\parallel})$ both exhibit a foreground wedge similar to the right panel; however, there are differences in details. In the left panel, we have a large A3 region $(k_{1\parallel} > [k_{1\parallel}]_{\rm H})$ that has a relatively low level of foreground contamination. The region $[k_{1\parallel}]_{\rm H} \geqslant k_{1\parallel} > [k_{3\parallel}]_{\rm H}$ is A1, and the level of foreground contamination here is higher than that of the A3 region. The region $k_{1\parallel} \leqslant [k_{3\parallel}]_{\rm H}$ approximately denotes the boundary of the A0 region where we have the highest level of foreground contamination. In the middle panel, we have $k_{3\parallel} = 0$ throughout, which is always inside the foreground wedge. Here, the region $k_{1\parallel} > [k_{1\parallel}]_{\rm H}$ is A2, for which the level of foreground contamination is larger compared to the A3 region in the left panel. The region $k_{1\parallel} \leqslant [k_{1\parallel}]_{\rm H}$ is A0, and we have a high level of foreground contamination here. Furthermore, we observe a periodic pattern of horizontal streaks that extend across the $(k_{1\perp}, k_{1\parallel})$ plane. These streaks arise from the regular pattern of missing frequency channels in the data, similar to the cylindrical PS.

The panels in the bottom row of Figure 5 show a section through the corresponding panels of the upper row. The right panel shows $|P(k_{1\perp}, k_{1\parallel})|$ as a function of $k_{1\parallel}$ at a fixed value of $k_{1\perp} = 0.021\,{\rm Mpc}^{-1}$. Note the periodic pattern of spikes that occur at an interval $\delta k_{1\parallel} = 0.29\,{\rm Mpc}^{-1}$ that exactly matches the period (1.28 MHz) of the flagged frequency channels. The middle and left panels show $|B(k_{1\perp}, k_{1\parallel})|$ as a function of $k_{1\parallel}$ for a fixed value of $k_{1\perp} = 0.023\,{\rm Mpc}^{-1}$. The middle panel shows a periodic pattern of spikes, whose period $\delta k_{1\parallel} = 0.29\,{\rm Mpc}^{-1}$ exactly matches the PS. In contrast, the left panel shows spikes with a regular spacing of $\delta k_{1\parallel} = 0.145\,{\rm Mpc}^{-1}$, which is half that of the other two panels. Furthermore, the amplitude of the spikes varies periodically with a period $\delta k_{1\parallel} = 0.29\,{\rm Mpc}^{-1}$, i.e., every alternate spike is large. The pattern seen in the left panel actually arises from a combination of two sets of spikes, respectively corresponding to $k_{1\parallel}$ and $|k_{3\parallel}| = 2|k_{1\parallel}|$. The

**Table 1**
Number of Triangles Categorized by Level of Foreground Contamination

| Region | A0 | A1 | A2 | A3 |
|---|---|---|---|---|
| $N_{\rm tri}$ | $2.45 \times 10^9$ | $5.75 \times 10^9$ | $2.65 \times 10^{11}$ | $1.39 \times 10^{12}$ |
| Percentage | 0.15% | 0.35% | 15.91% | 83.60% |

**Notes.** A0, A1, A2, and A3 correspond to regions where zero, one, two, and three sides of a triangle avoid the foreground-dominated zone, respectively. The total number of triangles analyzed is $1.66 \times 10^{12}$.

findings here substantiate our interpretation of the top row of Figure 4, where we have interpreted the periodic square grid pattern that runs across the entire $(k_{1\parallel}, k_{2\parallel})$ plane as arising from the periodic pattern of missing frequency channels.

We now consider the bottom panels of Figure 5 to compare the amplitudes of $|B(k_{1\perp}, k_{1\parallel})|$ at different $k_{1\parallel}$. In both the left and middle panels, the range of $k_{1\parallel} \approx 0$ is in the A0 region, and we have a peak value of $\sim 10^{24}$ mK$^3$ Mpc$^6$ for both panels. The range of $k_{1\parallel} \geqslant 0.5$ Mpc$^{-1}$ is in the A3 region for the left panel, while it is in the A2 region in the middle panel. Leaving aside the spikes, we see that $|B(k_{1\perp}, k_{1\parallel})|$ has values $\sim 10^{16}$–$10^{17}$ mK$^3$ Mpc$^6$ in the left panel, whereas it has values $\sim 10^{19}$ mK$^3$ Mpc$^6$ in the right panel. The amplitude of the spikes is also smaller in the left panel ($\sim 10^{19}$ mK$^3$ Mpc$^6$) compared to the right panel ($\sim 10^{21}$ mK$^3$ Mpc$^6$).

Figure 5 clearly demonstrates a foreground wedge for the cylindrical BS, very similar to the cylindrical PS. We see that the level of foreground contamination successively decreases from region A0 to A3. We may interpret the A3 region, which has the least level of foreground contamination, as the EoR window for the cylindrical BS. However, the present data shows considerable leakage into the EoR window, and the situation is particularly aggravated by the periodic pattern of missing frequency channels that produces a periodic pattern of spikes across the EoR window.

### 3.4. The Spherical BS

In the final step of our analysis, we calculate the 3D spherical BS $\bar{B}(k_1, k_2, k_3)$ with $k_1 \geqslant k_2 \geqslant k_3$, where $k_1 = \sqrt{k_{1\perp}^2 + k_{1\parallel}^2}$, etc. Here, $(k_1, k_2, k_3)$ specify the lengths of the three sides of a triangle $(\boldsymbol{k}_1, \boldsymbol{k}_2, \boldsymbol{k}_3)$, which uniquely specify its shape and size. Note that it is necessary to also specify the orientation of the triangle with respect to the LoS in order to specify $B(k_{1\perp}, k_{2\perp}, k_{3\perp}, k_{1\parallel}, k_{2\parallel})$ the cylindrical BS.

Here, we adopt a convenient parameterization (S. Bharadwaj et al. 2020) for the triangle $(k_1, k_2, k_3)$, which uses the largest side $k_1$ to quantify the size and the two dimensionless parameters

$$\mu = -\frac{\boldsymbol{k}_1 \cdot \boldsymbol{k}_2}{k_1 k_2}, \quad t = \frac{k_2}{k_1} \tag{7}$$

to quantify the shape. The values of the parameters $(\mu, t)$ are confined to the range of

$$0.5 \leqslant \mu, t \leqslant 1 \text{ and } 2\mu t \geqslant 1. \tag{8}$$

Furthermore, $k_3 = k_1 \sqrt{1 + t^2 - 2\mu t}$. The orientation of the triangle with respect to the LoS is specified by a unit vector $\hat{\boldsymbol{p}}$, for which

$$k_{1\parallel} = k_1 p_z, \; k_{2\parallel} = k_1 t \, (-\mu \, p_z + \sqrt{1 - \mu^2} \, p_x). \tag{9}$$

In this parameterization, the cylindrical BS can be expressed as

$$B(k_1, \mu, t, \hat{\boldsymbol{p}}) \equiv B(k_{1\perp}, k_{2\perp}, k_{3\perp}, k_{1\parallel}, k_{2\parallel}), \tag{10}$$

which is a function of five independent parameters.

Redshift space distortion of the 21 cm signal introduces an anisotropy with respect to the LoS (S. Bharadwaj & S. S. Ali 2004), which causes the BS to depend on the orientation of the triangle. It is possible to quantify this by decomposing the BS in terms of a spherical harmonic $Y_l^m(\hat{\boldsymbol{p}})$ (R. Scoccimarro et al. 1999; S. Bharadwaj et al. 2020), and we have the BS multipoles

$$\bar{B}_l^m(k_1, \mu, t) = \sqrt{\frac{2l+1}{4\pi}} \int [Y_l^m(\hat{p})]^* \, B(k_1, \mu, t, \hat{\boldsymbol{p}}) \, d\Omega_{\hat{p}}. \tag{11}$$

Theoretical predictions for the higher multipoles have been analyzed earlier (S. Bharadwaj et al. 2020; A. Mazumdar et al. 2020). In a recent work, S. S. Gill & S. Bharadwaj (2025a) have implemented a brisk estimator for the angular multipoles of the BS. The present work follows S. S. Gill & S. Bharadwaj (2025a) for a discrete implementation of Equation (11); however the analysis here is restricted to $\bar{B}_0^0(k_1, \mu, t)$ the monopole, which we denote using

$$\bar{B}(k_1, \mu, t) \equiv \bar{B}_0^0(k_1, \mu, t), \tag{12}$$

and refer to as the spherical BS in the rest of this paper. For each estimate of the spherical BS, we also compute $N_{\rm tri}(k_1, \mu, t)$, the number of $(\boldsymbol{k}_1, \boldsymbol{k}_2, \boldsymbol{k}_3)$ triangles that contribute to the estimate.

The estimated values of $\bar{B}(k_1, \mu, t)$ are irregularly distributed and do not uniformly sample $(k_1, \mu, t)$. We perform an additional binning in the $(k_1, \mu, t)$ space to obtain a more uniform coverage and also enhance the signal-to-noise ratio. The $k_1$ range of [0.002 Mpc$^{-1}$, 4.624 Mpc$^{-1}$] is divided into 20 equal logarithmically spaced bins, while the $\mu$ and $t$ ranges are each divided into five linearly spaced bins. The bin-averaged values of $k_1$ for which the BS estimates are obtained span the range of [0.005 Mpc$^{-1}$, 3.88 Mpc$^{-1}$]. Within each bin, we compute a weighted average of the estimated spherical BS using the number of triangles as weights. We then have uniformly spaced estimates of $\bar{B}(k_1, \mu, t)$ and $N_{\rm tri}(k_1, \mu, t)$. Instead of the spherical BS, we consider the mean-cube brightness temperature fluctuations,

$$\Delta^3(k_1, \mu, t) = (2\pi^2)^{-2} \, k_1^6 \, \bar{B}(k_1, \mu, t) \, , \tag{13}$$

for which the results are shown in the next section. We have used noise-only simulations to predict the expected statistical fluctuations in the estimated values of $\Delta^3(k_1, \mu, t)$ shown here.

## 4. Results

Figure 6 shows $|\Delta^3(k_1)|$, which corresponds to $|\Delta^3(k_1, \mu, t)|$ as a function of $k_1$ for fixed $(\mu, t)$. Here we show results for two fixed values $(\mu, t) \approx (0.5, 1)$ and $(1, 1)$, which respectively correspond to equilateral triangles (left panel) and squeezed triangles (right panel). The solid black curve (A0+A1+A2 +A3) shows $|\Delta^3(k_1)|$ estimated using all available values of $B(k_{1\perp}, k_{2\perp}, k_{3\perp}, k_{1\parallel}, k_{2\parallel})$, including those in the A0 region, which we know for sure to have a high level of foreground contamination. We see that the estimates span the range of $k_1 \in [0.005, 0.258]$ Mpc$^{-1}$ and $k_1 \in [0.012, 3.88]$ Mpc$^{-1}$ for

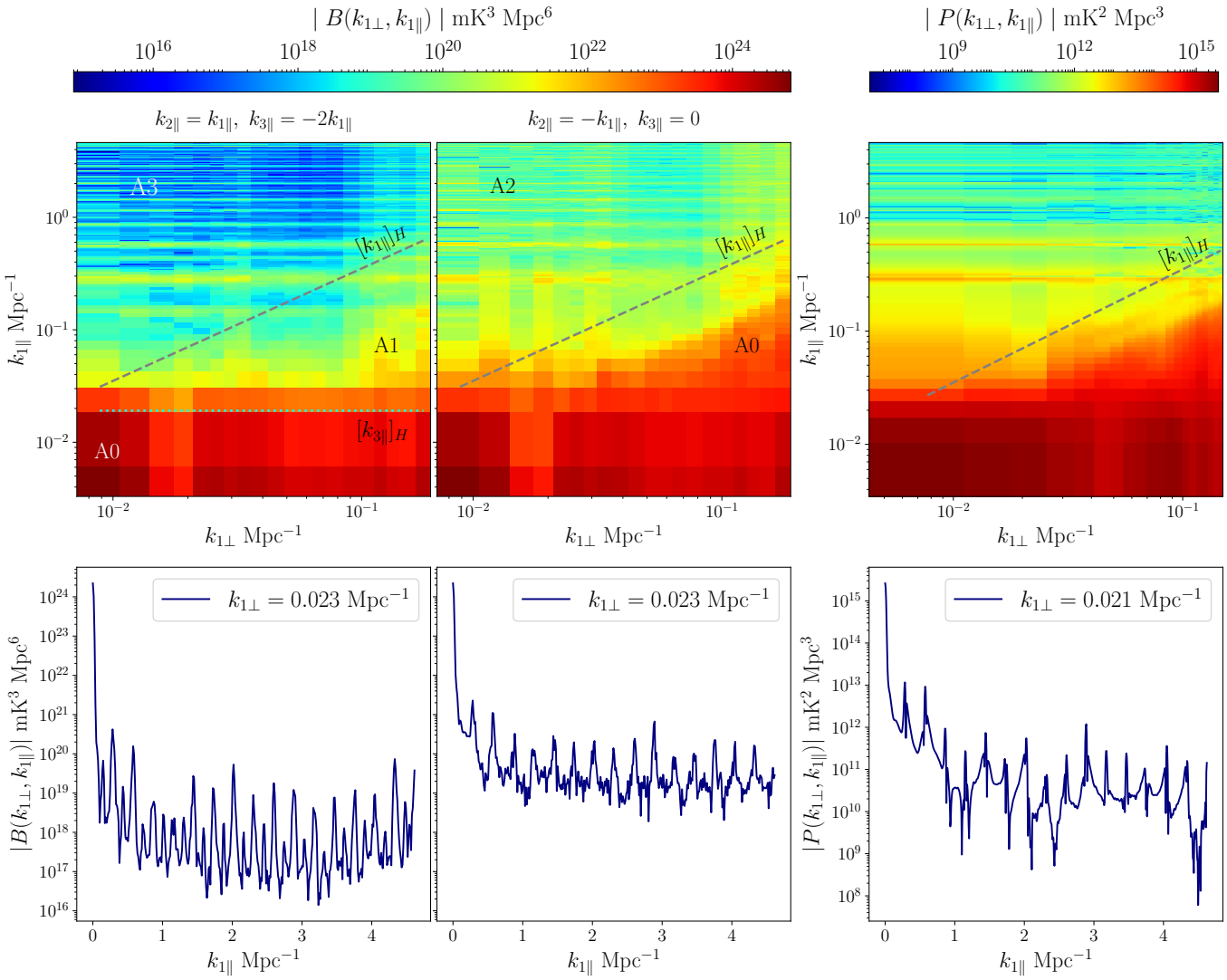


**Figure 5.** The top row shows $|B(k_{1\perp}, k_{1\parallel})|$, which is the magnitude of the 3D cylindrical BS $|B(k_{1\perp}, k_{2\perp}, k_{3\perp}, k_{1\parallel}, k_{2\parallel})|$ for squeezed triangles ($k_{1\perp} \approx k_{2\perp}$, $k_{3\perp} \to 0$) with the constraints $k_{1\parallel} = k_{2\parallel}$ and $k_{1\parallel} = -k_{2\parallel}$ for the left and center panels, respectively. The top-right panel shows $|P(k_{1\perp}, k_{1\parallel})|$ the cylindrical PS for the same data from K. M. A. Elahi et al. (2025). In each panel, the dashed line shows the predicted foreground wedge boundary $[k_{1\parallel}]_H = [r/(r'\Delta\nu_c)]k_{1\perp}$, whereas the dotted line in the left panel shows $[k_{3\parallel}]_H$ corresponding to the minimum value of $k_{3\perp}$ (= 0.005 Mpc$^{-1}$). The panels in the bottom row show 1D sections through the respective panels of the upper row, at $k_{1\perp} \approx 0.023$ Mpc$^{-1}$ for the BS and $k_{1\perp} \approx 0.021$ Mpc$^{-1}$ for the PS.

equilateral and squeezed triangles, respectively. Note that we do not have squeezed triangles ($k_3 \ll k_1 \approx k_2$) for a few of the smallest $k_1$. Furthermore, the large $k$ are mainly dominated by $k_\parallel$ as against $k_\perp$, and the condition $k_{3\parallel} = -(k_{1\parallel} + k_{2\parallel})$ precludes equilateral triangles for large $k_1$. We find that $|\Delta^3(k_1)|$ shows very similar behavior for equilateral and squeezed triangles. In both cases, $|\Delta^3(k_1)| \approx 10^{10}$ mK$^3$ at the smallest $k_1$, and the amplitude increases monotonically with $k_1$ until $k_1 \approx 0.2$ Mpc$^{-1}$, where $|\Delta^3(k_1)| \approx 10^{16}$ mK$^3$ and $10^{17}$ mK$^3$ for equilateral and squeezed triangles, respectively. Beyond this, in both cases, $|\Delta^3(k_1)|$ drops abruptly by 1 order of magnitude at $k_1 \approx 0.3$ Mpc$^{-1}$. The equilateral triangles do not extend to larger $k_1$; for squeezed triangles, $|\Delta^3(k_1)|$ continues to increase and reaches $\approx 10^{20}$ mK$^3$ at $k_1 \approx 4$ Mpc$^{-1}$. Note the abrupt change in the behavior of $|\Delta^3(k_1)|$ at $k_1 \approx 0.3$ Mpc$^{-1}$: not only does the value fall by an order of magnitude, but the slope also changes at larger $k_1$.

The solid red curve in the right panel of Figure 6 shows $|\Delta^2(k_1)|^{3/2}$, where the mean-square brightness temperature fluctuation $\Delta^2(k_1) = (2\pi^2)^{-1} k_1^3 P(k_1)$ is calculated using $P(k_1)$ the spherical PS estimated using all the $(k_{1\perp}, k_{1\parallel})$ modes shown in Figure 5. We see that at small $k_1$, the values of $|\Delta^2(k_1)|^{3/2}$ are comparable to those of $|\Delta^3(k_1)|$. In addition, $|\Delta^2(k_1)|^{3/2}$ and $|\Delta^3(k_1)|$ both show very similar behavior in which the values increase with $k_1$ until $k_1 \approx 0.2$ Mpc$^{-1}$, drop abruptly at $k_1 \approx 0.3$ Mpc$^{-1}$, and then increase again with a different slope. The large $k_1$ modes are predominantly outside the foreground wedge, and in all cases, we may associate the transition at $k_1 \approx 0.2$–$0.3$ Mpc$^{-1}$ with a crossing of the wedge boundary (Figure 5). For both the PS and the BS, the results are strongly foreground dominated at $k_1 \leqslant 0.2$ Mpc$^{-1}$, while we have a significant number of modes (triangles) in the EoR window for larger $k_1$.

We next attempt to mitigate foreground contamination in the estimated spherical BS by adopting the foreground avoidance technique. We have seen that A0 is the most severely affected by foregrounds. In both panels, the blue dotted line (A1+A2 +A3) shows $|\Delta^3|$ when A0 is excluded. This eliminates the estimates at small $k_1$, and now we only have estimates of $|\Delta^3|$ for $k_1 > 0.02$ Mpc$^{-1}$. We find some reduction in the values of

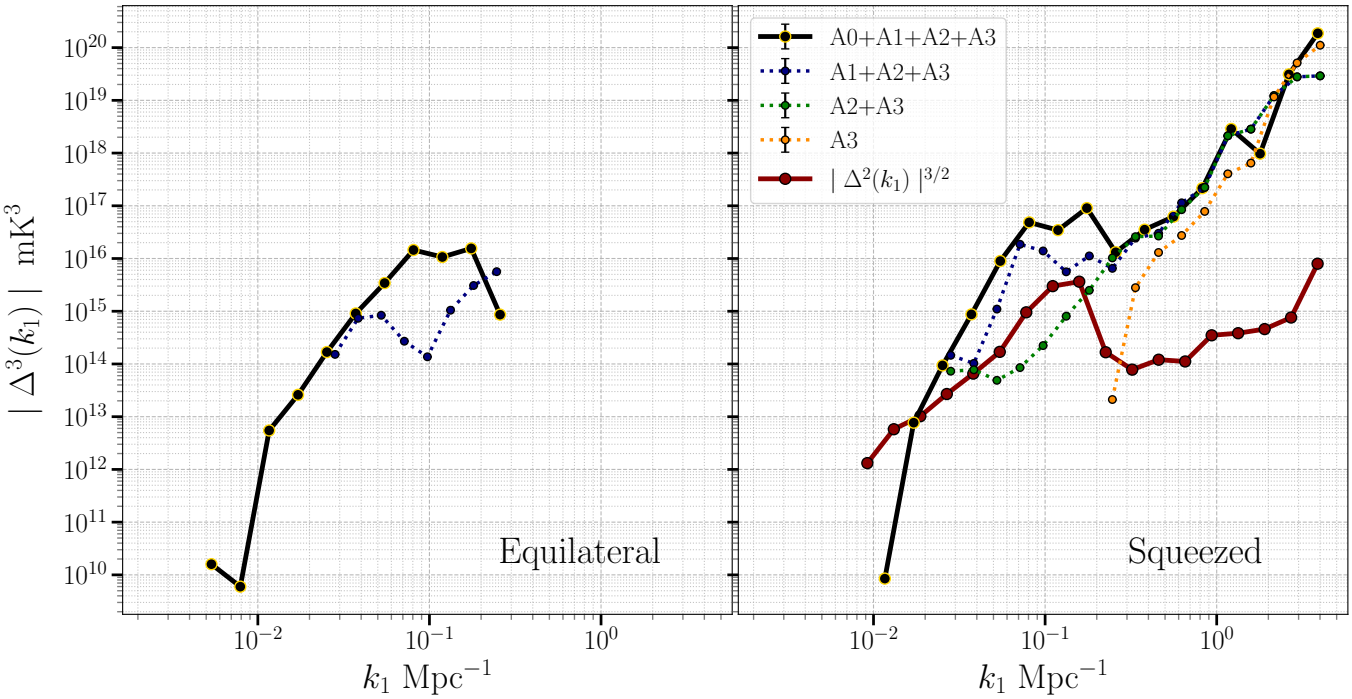


**Figure 6.** Mean-cube brightness temperature fluctuations, $\Delta^3(k_1)$, for equilateral triangles ($k_1 \approx k_2 \approx k_3$) in the left panel and squeezed triangles ($k_1 \approx k_2$, $k_3 \to 0$) in the right panel. The solid black lines show results with no foreground avoidance (A0+A1+A2+A3). The dotted colored lines show results for various foreground avoidance scenarios, as indicated in the figure legend. The solid red line shows $|\Delta^2(k_1)|^{3/2}$, where $\Delta^2(k_1)$ is the mean-square brightness temperature fluctuation from K. M. A. Elahi et al. (2025), who have analyzed the same data.

$|\Delta^3|$ in the range of $k_1 < 0.3\,\mathrm{Mpc}^{-1}$, but not beyond. In the subsequent cases, we only have estimates of $|\Delta^3|$ for squeezed triangles. For the green dotted curve (A2+A3), there is some further reduction at $k_1 < 0.3\,\mathrm{Mpc}^{-1}$, but not beyond. The yellow dotted curve (A3) shows the most conservative situation, which only considers triangles whose three sides are all outside the foreground wedge. At $k_1 \approx 0.3\,\mathrm{Mpc}^{-1}$, which is the smallest $k_1$ where we have an estimate, we find a substantial reduction in the value of $|\Delta^3|$ from $1.31 \times 10^{16}\,\mathrm{mK}^3$ (A0+A1+A2+A3) to $2.12 \times 10^{13}\,\mathrm{mK}^3$ (A3). In this case, foreground avoidance reduces the value of the spherical BS by a factor of ≈620, that is, a reduction in foreground contamination by nearly 3 orders of magnitude. This large reduction indicates that at this $k_1$, prior to foreground avoidance, $|\Delta^3|$ has a substantial contribution from A0, A1, and A2 triangles that contain a large level of foreground contamination. We avoid the contribution from these triangles when we consider only A3. Considering larger $k_1$ (>0.3 $\mathrm{Mpc}^{-1}$), here also we find a reduction in the values of $|\Delta^3|$; however, the effect is relatively small. This indicates that the triangles here are mostly in the A3 region, both before and after foreground avoidance.

The $1\sigma$ error bars corresponding to system noise have been shown for all the results in Figure 6. However, these are too small to be visible here. Based on this, we conclude that all the BS (or $|\Delta^3|$) values shown here are foreground dominated. Although foreground avoidance leads to a substantial improvement in at least one case shown here, it fails to completely eliminate foreground contamination from the final estimated value. This indicates substantial leakage into the EoR window, as is visible in Figure 5. This issue is particularly aggravated by the periodic pattern of missing frequency channels.

Figure 7 shows $|\Delta^3(k_1, \mu, t)|$ as a function of $k_1$, where each panel corresponds to a different value of $(\mu, t)$. As mentioned earlier, the allowed range of $(\mu, t)$ (Equation (8)) has been divided into $5 \times 5$ bins, not all of which are within the allowed region shown in the reference plot at the bottom-left corner of the figure. Each panel corresponds to a different triangle shape, as indicated in the reference plot and discussed in detail in S. Bharadwaj et al. (2020). Note that the isosceles triangles have been classified as L or S depending on whether their two large sides or small sides are equal. The equilateral and squeezed triangles, which have already been discussed in detail, are shown respectively in the top-left and top-right panels. The bottom-right panel shows the results for stretched triangles where $k_1/2 \approx k_2 \approx k_3$.

The black solid lines in the different panels of Figure 7 show $|\Delta^3(k_1, \mu, t)|$ obtained by combining all available triangles (A0 +A1+A2+A3). We have also tried applying foreground avoidance. However, this discards a large region of the $(k_1, \mu, t)$ space, which is why we have not shown the results here. The $k_1$ range across which we have estimates of $|\Delta^3|$ varies with $(\mu, t)$. We see that the results shown in the different panels are broadly very similar to those shown in Figure 6, which has already been discussed in detail. At small $k_1$, $|\Delta^3(k_1)|$ increases with $k_1$, exhibits a dip around $k_1 \approx 0.2$–$0.3\,\mathrm{Mpc}^{-1}$, and then increases again with a different slope at larger $k_1$. Each panel shows two reference lines, one vertical at $k_1 = 0.025\,\mathrm{Mpc}^{-1}$ and the other horizontal at $|\Delta^3| = 10^{14}\,\mathrm{mK}^3$. These lines illustrate that at small $k_1$, $|\Delta^3|$ has roughly the same value in all the panels. In most cases, $|\Delta^3|$ ranges from $10^{13}$ to $10^{17}\,\mathrm{mK}^3$ at small $k_1$. Note that the available $k_1$ range depends on $(\mu, t)$ (the triangle shape), with the squeezed triangle spanning the widest $k_1$ range, followed by the other linear (degenerate) triangle along $\mu \approx 1$. The

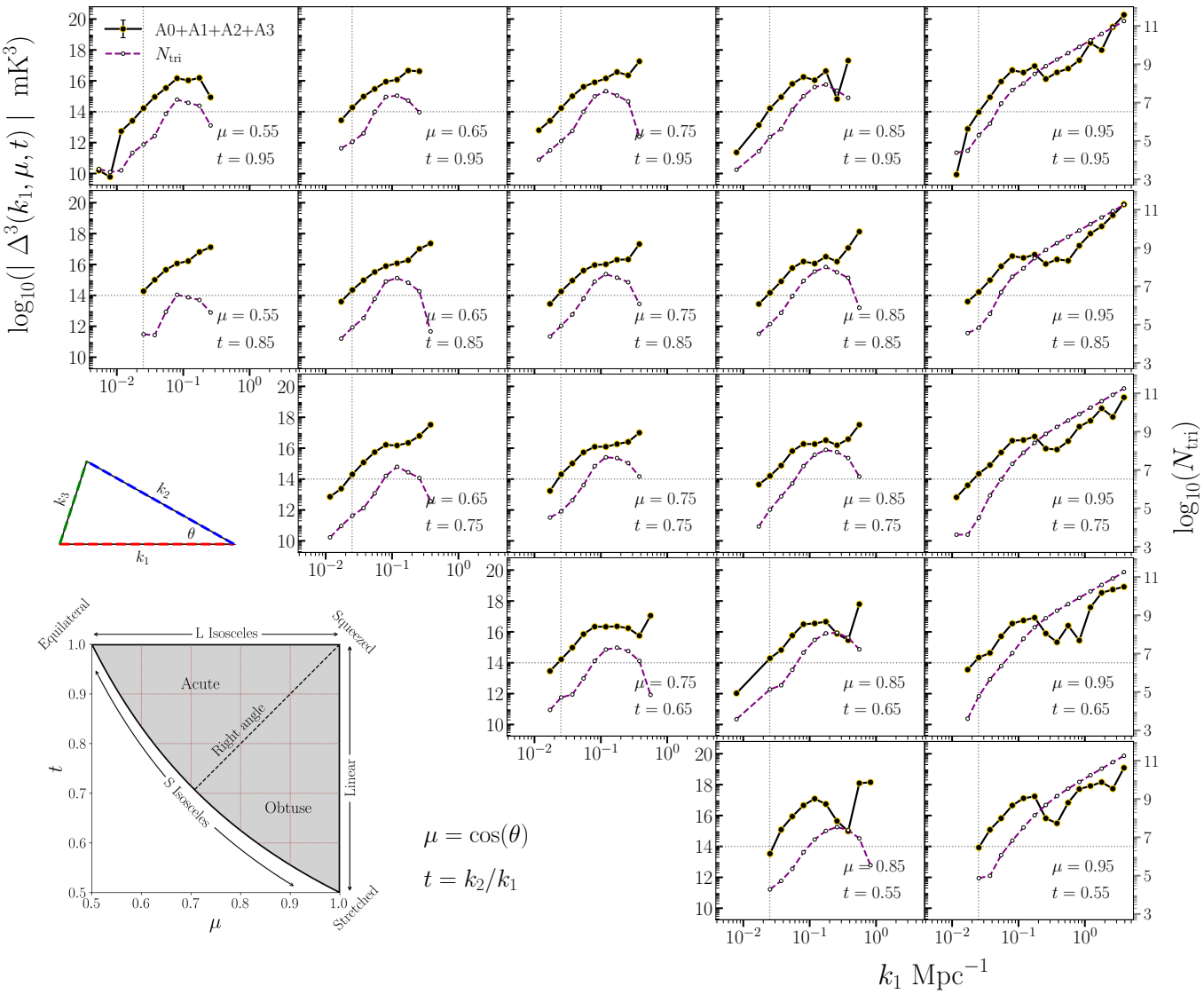


**Figure 7.** $|\Delta^3(k_1, \mu, t)|$ for triangles of all possible sizes ($k_1$) and shapes ($\mu$, $t$) available from this data. Each panel, which shows $|\Delta^3(k_1)|$ as a function of $k_1$, corresponds to a different shape ($\mu$, $t$), as indicated by the inset figure in the lower-left corner and detailed in S. Bharadwaj et al. (2019). The top-left and top-right panels, respectively, correspond to the equilateral ($\mu = 0.55$, $t = 0.95$) and squeezed ($\mu = 0.95$, $t = 0.95$) triangles for which the results have been shown in Figure 6. The results shown in black solid lines do not incorporate any foreground avoidance (A0+A1+A2+A3). The black dashed lines, $k_1 = 0.025$ Mpc$^{-1}$ (vertical) and $|\Delta^3| = 10^{14}$ mK$^3$ (horizontal), are shown for reference. The purple dashed lines show $N_{\rm tri}(k_1, \mu, t)$, the number of ($\boldsymbol{k}_1$, $\boldsymbol{k}_2$, $\boldsymbol{k}_3$) triangles in each ($k_1$, $\mu$, $t$) bin.

value of $|\Delta^3|$ reaches $\approx 10^{20}$ mK$^3$ at $k_1 \approx 4$ Mpc$^{-1}$, which is the largest value of $k_1$ here.

The purple dashed line in each panel shows $N_{\rm tri}(k_1, \mu, t)$, which is the number of ($\boldsymbol{k}_1$, $\boldsymbol{k}_2$, $\boldsymbol{k}_3$) triangles contained in the corresponding ($k_1$, $\mu$, $t$) bin. We see that $N_{\rm tri}$ spans a wide range of values from $\sim 10^3$ to $\sim 10^{11}$, as indicated on the right side of the figure. In all cases, $N_{\rm tri}$ is small at low $k_1$ and initially increases with $k_1$. For most triangle shapes, excluding the linear ones ($\mu \approx 1$), $N_{\rm tri}$ peaks at $\sim 10^8$ around $k_1 \approx 0.1$–$0.3$ Mpc$^{-1}$ and subsequently decreases at larger $k_1$. For $\mu \approx 1$, the value of $N_{\rm tri}$ increases monotonically to $\sim 10^{11}$ at the largest $k_1$.

The $1\sigma$ error bars shown in all the panels of Figure 7 are too small to be visible, and we interpret the results shown here as foreground dominated. We use these foreground-dominated estimates to place upper limits on $\Delta^3$ for the EoR 21 cm signal. We find the most stringent upper limits at the smallest values of $k_1$ for equilateral and squeezed triangles, which are tabulated in Table 2. The $2\sigma$ upper limit $\Delta^3_{\rm UL}$ has values of $(1.81 \times 10^3)^3$ mK$^3$ at $k_1 = 0.008$ Mpc$^{-1}$ and $(2.04 \times 10^3)^3$ mK$^3$ at $k_1 = 0.012$ Mpc$^{-1}$ for equilateral and squeezed triangles, respectively. The complete set of estimates and upper limits for all $|\Delta^3(k_1, \mu, t)|$ shown in the different panels of Figure 7 is available as a text file accessible via the link in the Data Availability section.

The $z \approx 8$ EoR 21 cm signal is predicted to be $\Delta^3 \approx 10^3$–$30^3$ mK$^3$ within the range of $k_1 \approx 0.29$–$2.48$ Mpc$^{-1}$ (S. S. Gill et al. 2024), which is approximately 13–15 orders of magnitude smaller than the upper limits obtained here in the same $k_1$ range. As discussed in Figure 6, for a few $k_1$ bins, it is possible to reduce the upper limits on $\Delta^3$ by 2–3 orders of magnitude if we adopt foreground avoidance. In the present work, we do not consider foreground removal for the different ($\mu$, $t$) bins shown in Figure 7. In the future, we plan to consider the issue of foreground mitigation in more detail.

**Table 2**
The Measured $\Delta^3(k_1, \mu, t)$, Corresponding $1\sigma$ Systematical Uncertainties, $2\sigma$ Upper Limit $\Delta^3_{\rm UL}$, and Number of Triangles $N_{\rm tri}$

| Shape | Size | BS | | | Triangles |
|---|---|---|---|---|---|
| | $k_1$ (Mpc$^{-1}$) | $\Delta^3$ (mK$^3$) | $1\sigma$ (mK$^3$) | $\Delta^3_{\rm UL}$ (mK$^3$) | $N_{\rm tri}$ |
| Equilateral ($\mu = 0.5$, $t = 0.95$) | 0.008 | $(1.81 \times 10^3)^3$ | $(3.48 \times 10^1)^3$ | $(1.81 \times 10^3)^3$ | $2.38 \times 10^3$ |
| Squeezed ($\mu = 0.95$, $t = 0.95$) | 0.012 | $(2.04 \times 10^3)^3$ | $(4.74 \times 10^1)^3$ | $(2.04 \times 10^3)^3$ | $2.44 \times 10^4$ |

**Notes.** The values are shown only for two triangle configurations—equilateral and squeezed—where the tightest upper limits $\Delta^3_{\rm UL}$ are obtained. The full set of estimates for all triangle types is provided through the link in the Data Availability section.

## 5. Summary and Conclusions

The EoR 21 cm signal is predicted to be highly non-Gaussian due to the presence of ionized bubbles (S. Bharadwaj & S. K. Pandey 2005). The PS, which is commonly employed to characterize the statistics of the EoR 21 cm signal, is insensitive to non-Gaussianity. The BS is the lowest-order statistic that is sensitive to non-Gaussianity. Here, we have used a recently developed visibility-based estimator (Paper II) to compute the $z = 8.2$ EoR 21 cm BS from a single pointing of the MWA drift-scan observations (A. K. Patwa et al. 2021).

In the first step of our analysis, we estimate the MABS $B_A(\ell_1, \ell_2, \ell_3, \Delta\nu_1, \Delta\nu_2)$ from gridded visibility data. The MABS, shown in Figures 2 and 3, is foreground dominated, and it has a peak value $\sim 10^6$ mK$^3$ at $\Delta\nu_1 = \Delta\nu_2 = 0$. The value of the MABS falls at larger $(\Delta\nu_1, \Delta\nu_2)$, and it drops to approximately one-sixth of the peak value at the largest frequency separation $\pm 15.36$ MHz. This behavior of the foreground signal is quite different from that expected for a cosmological 21 cm signal (Paper II), where the MABS is predicted to decorrelate rapidly with increasing frequency separation $(\Delta\nu_1, \Delta\nu_2)$, and have a value close to zero at frequency separations larger than $\pm 2$ MHz. Although the MWA data have a periodic pattern of missing frequency channels, we do not find any missing frequency separation $(\Delta\nu_1, \Delta\nu_2)$. However, as noted in Paper II, this introduces a periodic modulation in the sampling of the $(\Delta\nu_1, \Delta\nu_2)$ values. Note that our analysis assumes that the signal is ergodic along the LoS (frequency) direction. This may not be strictly valid across the relatively large bandwidth or redshift range considered here, and this may result in some signal loss in the estimated 21 cm BS. While this loss has been quantified for the PS (R. Mondal et al. 2018), its impact on the BS remains to be addressed in future work.

We have calculated the 3D cylindrical BS $B(k_{1\perp}, k_{2\perp}, k_{3\perp}, k_{1\parallel}, k_{2\parallel})$ by performing a 2D Fourier transform of the MABS with respect to $(\Delta\nu_1, \Delta\nu_2)$. The values of $B(k_{1\perp}, k_{2\perp}, k_{3\perp}, k_{1\parallel}, k_{2\parallel})$, shown in Figure 4, peak around $k_{1\parallel} = k_{2\parallel} = 0$, and decline rapidly with increasing $(k_{1\parallel}, k_{2\parallel})$. In addition, we observe a square grid pattern that runs across the entire $(k_{1\parallel}, k_{2\parallel})$ plane. This 2D oscillatory pattern has a period of $\delta k_\parallel = 0.29$ Mpc$^{-1}$, which exactly matches the period of the pattern of missing frequency channels in the MWA data. Furthermore, we notice three bands that run across the $(k_{1\parallel}, k_{2\parallel})$ plane, which we identify as the foreground wedge corresponding to $(k_{1\perp}, k_{1\parallel})$, $(k_{2\perp}, k_{2\parallel})$, and $(k_{3\perp}, k_{3\parallel})$, respectively. Based on this, we partition the entire $(k_{1\parallel}, k_{2\parallel})$ plane into four distinct regions, namely A0, A1, A2, and A3. In A3, all three modes $(k_{1\perp}, k_{1\parallel})$, $(k_{2\perp}, k_{2\parallel})$, and $(k_{3\perp}, k_{3\parallel})$ avoid the respective foreground wedge, whereas only two of the modes avoid the foreground wedge for A2, and so forth. We expect A3 to have the lowest level of foreground contamination in the cylindrical BS $B(k_{1\perp}, k_{2\perp}, k_{3\perp}, k_{1\parallel}, k_{2\parallel})$, and this is expected to increase as we go from A3 to A0.

Figure 5, which shows $B(k_{1\perp}, k_{1\parallel})$ the cylindrical BS for two specific triangle configurations, clearly illustrates the foreground wedge. This figure also shows $P(k_{1\perp}, k_{1\parallel})$, the cylindrical PS from K. M. A. Elahi et al. (2025), for exactly the same MWA data. The familiar foreground wedge is clearly visible in the $(k_{1\perp}, k_{1\parallel})$ plane for both $B(k_{1\perp}, k_{1\parallel})$ and $P(k_{1\perp}, k_{1\parallel})$. The BS $B(k_{1\perp}, k_{1\parallel})$ clearly shows the expected differences in the levels of foreground contamination in the regions A0, A1, A2, and A3. We identify A3, which has the lowest level of foreground contamination, as the EoR window for the BS. Both the PS and the BS exhibit a periodic pattern of spikes due to the periodic pattern of missing frequency channels. This extends across the entire $(k_{1\perp}, k_{1\parallel})$ plane, causing severe foreground leakage into the EoR window. Although we have illustrated the foreground wedge for only two specific triangle shapes here, we have verified that this feature is present across all possible triangle shapes.

The present analysis includes all possible triangles $(\boldsymbol{k}_1, \boldsymbol{k}_2, \boldsymbol{k}_3)$ that arise from the given data, which have a total number of $N_{\rm tri} = 1.66 \times 10^{12}$. Of these, approximately 83.6% are in the EoR window (A3 region, Figure 1). This bodes well for using foreground avoidance to mitigate foreground contamination for the 21 cm BS. However, we do not get any estimates at small $k_1$ if we restrict the analysis to the EoR window.

We finally use the measured $B(k_{1\perp}, k_{2\perp}, k_{3\perp}, k_{1\parallel}, k_{2\parallel})$ to evaluate the 3D spherical BS $\bar{B}(k_1, \mu, t)$, where $k_1$ and $(\mu, t)$, respectively, quantify the size and shape of the triangle $(k_1, k_2, k_3)$. Here we consider the mean-cube brightness temperature fluctuations $\Delta^3(k_1, \mu, t) = (2\pi^2)^{-2} k_1^6 \bar{B}(k_1, \mu, t)$, and we present results for $\Delta^3(k_1)$ as a function of $k_1$, considering triangles of all possible shapes $(\mu, t)$. Figure 6, which considers a variety of scenarios for foreground avoidance, shows $\Delta^3(k_1)$ for two particular triangle shapes, namely equilateral and squeezed. Figure 7 shows $\Delta^3(k_1)$ for triangles of all possible shapes, without incorporating foreground avoidance. We find that the available $k_1$ range varies with the triangle shape and the foreground avoidance scenario. We first consider the results without foreground avoidance (A0+A1+A2+A3). We have the broadest $k_1$ range of [0.012 Mpc$^{-1}$, 3.88 Mpc$^{-1}$] for squeezed triangles, although the lowest $k_1$ value (0.005 Mpc$^{-1}$) is achieved for equilateral triangles, for which the large $k_1$ (>0.3 Mpc$^{-1}$) are missing. We have the lowest value of $|\Delta^3(k_1)| \approx 10^{10}$ mK$^3$ at the smallest $k_1$ for equilateral and squeezed triangles (Table 2). The lowest values of $|\Delta^3(k_1)|$ are in the range of $10^{12}$–$10^{14}$ mK$^3$ for other shapes. We find the largest value of $|\Delta^3(k_1)| \approx 10^{20}$ mK$^3$ at 3.88 Mpc$^{-1}$ for squeezed triangles. In this study, we have also carried out simulations that only incorporate the expected system noise contribution to the

visibilities and analyzed these in exactly the same way as the actual data. These noise-only simulations were used to calculate $\sigma$ the rms statistical fluctuations expected in the estimated $\Delta^3$. The values of $\Delta^3$, $\sigma$, and the $2\sigma$ upper limits $\Delta^3_{\rm UL}$ for all ($k_1$, $\mu$, $t$) are available through the link provided in the Data Availability section. The estimated values of $\Delta^3$ are several orders of magnitude larger than those of $\sigma$, which leads us to believe that the present estimates are foreground dominated. We proceed to use these estimates to constrain the EoR 21 cm BS. The most stringent $2\sigma$ upper limits that we obtain are $\Delta^3_{\rm UL} = (1.81 \times 10^3)^3\,{\rm mK}^3$ at $k_1 = 0.008\,{\rm Mpc}^{-1}$ and $\Delta^3_{\rm UL} = (2.04 \times 10^3)^3\,{\rm mK}^3$ at $k_1 = 0.012\,{\rm Mpc}^{-1}$ for equilateral and squeezed triangles, respectively. Simulations predict the $z \approx 8$ EoR 21 cm signal to be $|\Delta^3| \approx 10^3$–$30^3\,{\rm mK}^3$ within the range of $k_1 \approx 0.29$–$2.48\,{\rm Mpc}^{-1}$ (S. S. Gill et al. 2024). Furthermore, $\Delta^3$ is predicted to be negative for small $k_1$ ($\lesssim 0.56\,{\rm Mpc}^{-1}$), which is an important signature of the distinct ionized bubbles that are present in the neutral H I background. The predicted EoR 21 cm BS is roughly 13–15 orders of magnitude smaller than the current upper limits obtained in the same $k_1$ range.

We have explored various foreground avoidance scenarios, for which the results for equilateral and squeezed triangles are shown in Figure 6. With foreground avoidance, we do not have estimates of $\Delta^3$ at small $k_1$. As a consequence, there is very little scope for using this technique for equilateral triangles. For squeezed triangles, considering only the EoR window, we have a substantial reduction (a factor of $\approx$620) in the foreground contamination at the smallest $k_1$ ($\approx 0.3\,{\rm Mpc}^{-1}$). However, we only have a small reduction at larger $k_1$, most probably due to the strong leakage into the EoR window due to the periodic pattern of missing frequency channels.

In summary, we have presented estimates of the H I 21 cm BS for a single PC from MWA drift-scan observations. The observation time for the data analyzed here, 17 minutes, is too short for a detection of the 21 cm BS, and we expect the estimates to be consistent with noise. However, we find that the estimated values presented here are much in excess of the noise predictions, indicating that they are foreground dominated. It may be possible to overcome this by first mitigating the level of foreground contamination in the visibility data by modeling the sky image, or using some frequency-based technique like smooth component filtering (K. M. A. Elahi et al. 2025), prior to estimating the 21 cm BS. We plan to attempt this in future work. We also plan to analyze all the PCs in the drift-scan observations, once we achieve some control over the foreground contamination. It will be possible to combine the estimates from the different PCs to reduce the noise level and obtain tighter constraints of the 21 cm BS once we have overcome the issue of foreground contamination.

## Acknowledgments

We acknowledge usage of the computing facilities in the Department of Physics, IIT Kharagpur.

## Data Availability

The data sets were derived from sources in the public domain (the MWA Data Archive: project ID G0031) available at the MWA ASVO Portal.[9] The data underlying Figure 7 is available on GitHub.[10]

## Appendix
## Effect of Gaussian Beam Approximation on MABS Normalization

The normalization factor that relates the three visibility correlations to the MABS is given by (refer to Equation (A11) of Paper I)

$$\mathcal{N} = Q^3 \Big[ \int d^2U_1' \int d^2U_2' \; \tilde{a}(\boldsymbol{U}_1 - \boldsymbol{U}_1') \times \tilde{a}(\boldsymbol{U}_2 - \boldsymbol{U}_2')\, \tilde{a}^*(\boldsymbol{U}_3 + \Delta\boldsymbol{U} - \boldsymbol{U}_3')\Big]\,, \tag{A1}$$

where $\tilde{a}(\boldsymbol{U})$ denotes the Fourier transform of the primary beam $A(\boldsymbol{\theta})$. Under the Gaussian beam approximation (Equation (6) in Paper I), we use

$$A_G(\boldsymbol{\theta}) = \exp\left[-\theta^2/\theta_0^2\right]. \tag{A2}$$

For this case, Equation (A1) can be analytically evaluated, which gives the normalization factor $\mathcal{N} = \frac{\pi\theta_0^2 Q^3}{3} \exp\left[-\pi^2\theta_0^2 \Delta U^2/3\right]$ that appears in Equation (2). In addition to this, we also consider a primary beam pattern that exhibits side lobes, similar to those expected in the actual MWA primary beam pattern. We adopt the form described in S. Chatterjee et al. (2024) (and also in Equation (5) of Paper I),

$$A(\boldsymbol{\theta}) = \mathrm{sinc}^2\left(\frac{\pi d\theta_x}{\lambda}\right) \quad \mathrm{sinc}^2\left(\frac{\pi d\theta_y}{\lambda}\right), \tag{A3}$$

for which Equation (A1) does not admit a simple analytical form. Here, we numerically evaluate this 4D integral and present the results in Figure 8, which compares the normalization factor obtained with the Gaussian beam approximation to that from the sinc$^2$ antenna pattern. The solid black curve shows the normalization factor $\mathcal{N}$ as a function of $\Delta U$ for a Gaussian beam, whereas the overlaid markers show the same for the sinc$^2$ beam pattern. We find that the two match closely, and they differ by no more than roughly 3% for $\Delta U \leqslant 1$, which is the relevant $\Delta U$ range. This analysis shows that the side lobes of the primary beam pattern do not contribute much to the normalization factor $\mathcal{N}$ that relates the three visibility correlations to the MABS.

[9] https://asvo.mwatelescope.org/

[10] https://github.com/sukhdeepsinghgill/EoR-21cm-Bispectrum/tree/main/Paper-1_PrelimResults

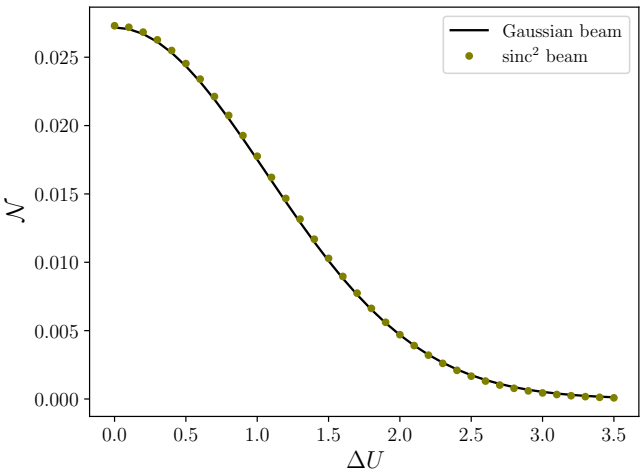


**Figure 8.** Shows how the normalization factor—relating the MABS to the three visibility correlations—varies with $\Delta U$. The solid black curve uses the Gaussian beam approximation (Equation (A2)), while the green markers correspond to normalization computed using the $\mathrm{sinc}^2$ beam profile (Equation (A3)).

## ORCID iDs

Sukhdeep Singh Gill https://orcid.org/0000-0003-1629-3357
Somnath Bharadwaj https://orcid.org/0000-0002-2350-3669
Khandakar Md Asif Elahi https://orcid.org/0000-0003-1206-8689
Shiv K. Sethi https://orcid.org/0000-0002-7737-1470
Akash Kumar Patwa https://orcid.org/0000-0002-6216-2430

## References

Abdurashidova, Z., Aguirre, J. E., Alexander, P., et al. 2022, ApJ, 925, 221
Ali, S. S., Bharadwaj, S., & Chengalur, J. N. 2008, MNRAS, 385, 2166
Bag, S., Mondal, R., Sarkar, P., Bharadwaj, S., & Sahni, V. 2018, MNRAS, 477, 1984
Bag, S., Mondal, R., Sarkar, P., et al. 2019, MNRAS, 485, 2235
Barnett, R., Warren, S. J., Becker, G. D., et al. 2017, A&A, 601, A16
Becker, R. H., Fan, X., White, R. L., et al. 2001, AJ, 122, 2850
Bharadwaj, S., & Ali, S. S. 2004, MNRAS, 352, 142
Bharadwaj, S., Mazumdar, A., & Sarkar, D. 2020, MNRAS, 493, 594
Bharadwaj, S., Pal, S., Choudhuri, S., & Dutta, P. 2019, MNRAS, 483, 5694
Bharadwaj, S., & Pandey, S. K. 2005, MNRAS, 358, 968
Bosman, S. E. I., Davies, F. B., Becker, G. D., et al. 2022, MNRAS, 514, 55
Bouwens, R. 2016, in Understanding the Epoch of Cosmic Reionization, Astrophysics and Space Science Library, ed. A. Mesinger, Vol. 423 (Cham: Springer), 111
Cain, C., Lopez, G., D'Aloisio, A., et al. 2025a, ApJ, 980, 83
Cain, C., Van Engelen, A., Croker, K. S., et al. 2025b, ApJL, 987, L29
Chatterjee, S., Elahi, K. M. A., Bharadwaj, S., et al. 2024, PASA, 41, e077
Choudhury, T. R., Puchwein, E., Haehnelt, M. G., & Bolton, J. S. 2015, MNRAS, 452, 261
Datta, A., Bowman, J. D., & Carilli, C. L. 2010, ApJ, 724, 526
DeBoer, D. R., Parsons, A. R., Aguirre, J. E., et al. 2017, PASP, 129, 045001
Elahi, K. M. A., Bharadwaj, S., Chatterjee, S., et al. 2025, MNRAS, 540, 2745
Fan, X., Strauss, M. A., Schneider, D. P., et al. 2003, AJ, 125, 1649
Furlanetto, S. R. 2006, MNRAS, 371, 867
Gill, S. S., & Bharadwaj, S. 2025a, PhRvD, 111, 043507
Gill, S. S., & Bharadwaj, S. 2025b, arXiv:2506.10526
Gill, S. S., Bharadwaj, S., Ali, S. S., & Elahi, K. M. A. 2025, ApJ, 979, 25
Gill, S. S., Pramanick, S., Bharadwaj, S., Shaw, A. K., & Majumdar, S. 2024, MNRAS, 527, 1135
Gupta, Y., Ajithkumar, B., Kale, H. S., et al. 2017, CSci, 113, 707
Harker, G. J. A., Zaroubi, S., Thomas, R. M., et al. 2009, MNRAS, 393, 1449
Hutter, A., Watkinson, C. A., Seiler, J., et al. 2020, MNRAS, 492, 653
Jensen, H., Laursen, P., Mellema, G., et al. 2013, MNRAS, 428, 1366
Kamran, M., Ghara, R., Majumdar, S., et al. 2021a, MNRAS, 502, 3800
Kamran, M., Ghara, R., Majumdar, S., et al. 2022, JCAP, 2022, 001
Kamran, M., Majumdar, S., Ghara, R., et al. 2021b, arXiv:2108.08201
Keating, L. C., Weinberger, L. H., Kulkarni, G., et al. 2020, MNRAS, 491, 1736
Komatsu, E., Smith, K. M., Dunkley, J., et al. 2011, ApJS, 192, 18
Koopmans, L., Pritchard, J., Mellema, G., et al. 2015, PoS, 215, 1
Kulkarni, G., Keating, L. C., Haehnelt, M. G., et al. 2019, MNRAS, 485, L24
Larson, D., Dunkley, J., Hinshaw, G., et al. 2011, ApJS, 192, 16
Loeb, A., & Zaldarriaga, M. 2004, PhRvL, 92, 211301
Ma, Q.-B., & Peng, L. 2023, MNRAS, 523, 640
Majumdar, S., Kamran, M., Pritchard, J. R., et al. 2020, MNRAS, 499, 5090
Majumdar, S., Pritchard, J. R., Mondal, R., et al. 2018, MNRAS, 476, 4007
Mazumdar, A., Bharadwaj, S., & Sarkar, D. 2020, MNRAS, 498, 3975
Melia, F. 2024, A&A, 689, A10
Mitra, S., Choudhury, T. R., & Ferrara, A. 2015, MNRAS, 454, L76
Mondal, R., Bharadwaj, S., & Datta, K. K. 2018, MNRAS, 474, 1390
Mondal, R., Bharadwaj, S., Majumdar, S., Bera, A., & Acharyya, A. 2015, MNRAS, 449, L41
Morales, M. F., Hazelton, B., Sullivan, I., & Beardsley, A. 2012, ApJ, 752, 137
Muñoz, J. B., Mirocha, J., Chisholm, J., Furlanetto, S. R., & Mason, C. 2024, MNRAS, 535, L37
Murmu, C. S., Datta, K. K., Majumdar, S., & Greve, T. R. 2024, JCAP, 2024, 032
Murray, S. G., & Trott, C. M. 2018, ApJ, 869, 25
Nuttall, A. H. 1981, ITASS, 29, 84
Ota, K., Iye, M., Kashikawa, N., et al. 2017, ApJ, 844, 85
Ouchi, M., Shimasaku, K., Furusawa, H., et al. 2010, ApJ, 723, 869
Papovich, C., Cole, J. W., Hu, W., et al. 2025, arXiv:2505.08870
Parsons, A. R., Pober, J. C., Aguirre, J. E., et al. 2012, ApJ, 756, 165
Patwa, A. K., Sethi, S., & Dwarakanath, K. S. 2021, MNRAS, 504, 2062
Planck Collaboration, Adam, R., Aghanim, N., et al. 2016, A&A, 596, A108
Planck Collaboration, Akrami, Y., Arroja, F., et al. 2020, A&A, 641, A9
Pritchard, J. R., & Loeb, A. 2012, RPPh, 75, 086901
Qin, Y., Mesinger, A., Prelogović, D., et al. 2025, PASA, 42, e049
Raste, J., Kulkarni, G., Watkinson, C. A., Keating, L. C., & Haehnelt, M. G. 2024, MNRAS, 529, 129
Runnholm, A., Hayes, M. J., Mehta, V., et al. 2025, ApJ, 984, 95
Saxena, A., Majumdar, S., Kamran, M., & Viel, M. 2020, MNRAS, 497, 2941
Scoccimarro, R., Couchman, H. M. P., & Frieman, J. A. 1999, ApJ, 517, 531
Shimabukuro, H., Yoshiura, S., Takahashi, K., Yokoyama, S., & Ichiki, K. 2015, MNRAS, 451, 467
Shimabukuro, H., Yoshiura, S., Takahashi, K., Yokoyama, S., & Ichiki, K. 2016, MNRAS, 458, 3003
Swarup, G., Ananthakrishnan, S., Kapahi, V. K., et al. 1991, CSci, 60, 95
Thompson, A. R., Moran, J. M., & Swenson, G. W., Jr. 2017, Interferometry and Synthesis in Radio Astronomy (3rd ed; Cham: Springer)
Tingay, S. J., Goeke, R., Bowman, J. D., et al. 2013, PASA, 30, e007
Tiwari, H., Shaw, A. K., Majumdar, S., Kamran, M., & Choudhury, M. 2022, JCAP, 2022, 045
Trenti, M., Stiavelli, M., Bouwens, R. J., et al. 2010, ApJL, 714, L202
Trott, C. M., Watkinson, C. A., Jordan, C. H., et al. 2019, PASA, 36, e023
Trott, C. M., Wayth, R. B., & Tingay, S. J. 2012, ApJ, 757, 101
Umeda, H., Ouchi, M., Nakajima, K., et al. 2024, ApJ, 971, 124
van Haarlem, M. P., Wise, M. W., Gunst, A. W., et al. 2013, A&A, 556, A2
Vedantham, H., Udaya Shankar, N., & Subrahmanyan, R. 2012, ApJ, 745, 176
Watkinson, C. A., Greig, B., & Mesinger, A. 2022, MNRAS, 510, 3838
Watkinson, C. A., & Pritchard, J. R. 2015, MNRAS, 454, 1416
Watkinson, C. A., Trott, C. M., & Hothi, I. 2021, MNRAS, 501, 367
White, R. L., Becker, R. H., Fan, X., & Strauss, M. A. 2003, AJ, 126, 1
Witstok, J., Jakobsen, P., Maiolino, R., et al. 2025, Natur, 639, 897
Yoshiura, S., Shimabukuro, H., Takahashi, K., et al. 2015, MNRAS, 451, 266
Zaroubi, S. 2013, The First Galaxies, Astrophysics and Space Science Library, Vol. 396 (Berlin: Springer), 45